INFRASOUND SIGNAL CHARACTERISTICS

OF SMALL EARTHQUAKES

by

John Mark Hale

A thesis submitted to the faculty of
The University of Utah
in partial fulfillment of the requirements for the degree of

Master of Science

in

Geophysics

Department of Geology and Geophysics

The University of Utah

August 2013

The University of Utah Graduate School

STATEMENT OF THESIS APPROVAL

The following faculty members served as the supervisory committee chair and

members for the thesis of_____John Mark Hale_____.

Dates at right indicate the members' approval of the thesis.

_____Michael S. Thorne_____, Chair   __05/31/2013_____
                                                         Date Approved

_____Kristine L. Pankow_____, Member   __05/31/2013_____
                                                         Date Approved

_____Keith D. Koper_____, Member   __05/31/2013_____
                                                         Date Approved

The thesis has also been approved by_____D. Kip Solomon_____,

Chair of the Department of_____Geology and Geophysics_____

and by Donna M. White, Interim Dean of The Graduate School.

ABSTRACT

The University of Utah Seismograph Stations recorded 293 earthquakes ($3.0 \leq M \leq 5.9$) between April 17, 2007 and June 30, 2012. During this time, four-element infrasound data were collected from three permanent (NOQ, BGU, and EPU; installed 2006 – 2007) and six temporary (BRP, WMU, HWU, FSU, LCM, and PSU; installed summer of 2010) seismo-acoustic arrays. Unique epicentral infrasound observations from nine earthquakes with M 3.6 – 5.9 are identified and characterized. The detections were recorded from normal, oblique normal, and strike-slip faulting earthquakes at distances of 156 – 695 km and depths of 5 – 12 km. We use ray-tracing through ground-to-space atmospheric models from the epicenters to each array to determine the atmospheric turning altitude and associated wind velocities. Distance and wind corrected amplitudes match previously determined scaling relations. However, the duration observations from smaller magnitude earthquakes suggest the possibility of an additional scaling relation for events $M < 4.6$. This possible change in duration scaling relation is inconsistent with the hypothesis that infrasound duration scales with the areal extent of the epicentral region subjected to a threshold peak ground acceleration. The predicted ground motions show that the area subject to the threshold increases more rapidly with increased magnitudes. Overall, the small percentage of infrasound detections from the total possible suggests that infrasound is not a robust method of detecting and characterizing small earthquake sources.

This work is dedicated to the love of my life, Tessa, who taught me to be willing to let go of a lifetime of self-doubt in order to create room for the confidence necessary to propel my future aspirations. She is the most amazing person that I have ever known.

Thank you.

TABLE OF CONTENTS

LIST OF FIGURES

LIST OF TABLES

ACKNOWLEDGEMENTS

Thank you to my amazing wife, Tessa, for her love, support, and patience throughout this research. This would not have been possible without her and I will never be able to fully express my love and gratitude. I would also like to thank my friends and family for their understanding of my relative absence during the past few years, including many missed parties, gatherings, and milestones.

Tremendous thanks goes to Kristine L. Pankow for her relentless guidance and dedication to this project and those of all her students. Her focused attention to detail while maintaining a perspective for the broader-scope of the research is a trait that I strive to achieve. Her mentorship has been invaluable and I will be forever grateful for having received it.

Michael Thorne has been instrumental in this research. Without his programming expertise and tutelage, this research would have been a far more daunting task. His exemplary teaching style should be a model for any professor seeking to inspire scientists. His passion displayed for teaching and research inspires me to be a better scientist.

Keith Koper is a tremendous resource, teacher, and a great leader. His support and encouragement for my research and education is greatly appreciated. I look forward to many years of working with him and contributing to his research in any way.

CHAPTER 1

INTRODUCTION

1.1 Significant Earthquake Infrasound Research

Large earthquakes are one of the most powerful sources of infrasound. The seismic waves' excitation of the surface and topography in the immediate region continually exceeding the ground motion threshold for infrasound discussed in Chapter 5, known as epicentral infrasound propagates at $0.02 - 10$ Hz through ducts formed in the atmosphere (Drob *et al.*, 2003). These infrasound signals are observable on microphones and microbarometers at distances of hundreds to thousands of kilometers from the source region. Benioff and Gutenberg (1939) first observed earthquake-generated infrasound from earthquakes located in California. More recently, infrasound has been detected from several large earthquakes, including the $M_W7.9$ Denali fault earthquake in Alaska (Le Pichon *et al.*, 2002 and Olson *et al.*, 2003), the $M_W7.8$ Tarapaca, Chile earthquake (Le Pichon *et al.*, 2006), the $M_W8.3$ and $M_W7.4$ Tokachi-Oki earthquake and aftershock (Kim *et al.*, 2004), and most recently, the $M_W9.0$ Tohoku-Oki earthquake in Japan (Garcia *et al.*, 2013).

Infrasound has also been observed from smaller earthquakes. For example, Green *et al.* (2009) observed directional infrasound generated by an $M_L4.3$ earthquake resonating the coastal cliffs near Folkestone, United Kingdom. Arrowsmith *et al.* (2012a) reported on infrasound generated from the epicentral region of the $M_W4.5$ earthquake

near Circleville, Utah.

These previous efforts provide examples of the three types of infrasound generation from earthquakes described by Cook (1971): 1) local infrasound is caused by seismic waves propagating through the array region disturbing the infrasound sensors; 2) epicentral infrasound which is caused by the seismic waves' excitation of the surface and topography in the epicentral region is responsible for most earthquake-generated infrasound; and 3) diffracted infrasound (or 'secondary infrasound') occurs in regions far from the epicenter when passing seismic waves interact with topographic features, generating an infrasonic signal that can be recorded after local infrasound and often before epicentral infrasound.

In an analysis of multiple earthquakes, Mutschlecner and Whitaker (2005; henceforth MW05) focus on epicentral infrasound observations from 31 earthquakes (4.4 $\leq M_L \leq 7.5$) recorded on acoustic arrays operated by Los Alamos National Laboratory from 1983 – 2003. These observations served to identify preliminary earthquake scaling relationships between seismic magnitude and either the log of epicentral infrasound amplitudes (corrected for stratospheric winds and normalized for distance) or the log of the signal duration. MW05 additionally proposed that a minimum peak surface acceleration threshold between 10 and 20 cm s^{-2} exists for atmospheric infrasound generation. The amplitude and duration scaling relations of MW05 were confirmed by Le Pichon *et al.* (2006) for earthquakes up to M8.5 using infrasound observations from 12 earthquakes occurring in 2001 – 2005. It is evident from these previous studies that at least some earthquakes generate infrasound and that relations exist between infrasound amplitude and duration versus magnitude.

1.2 Remaining Questions and Objectives

Several questions regarding earthquake-generated infrasound remain unanswered. In this study, we address the following questions:

Why do some earthquakes generate infrasound while others seemingly do not?

Do small earthquakes adhere to the amplitude and duration relations first identified by MW05?

Is earthquake-generated infrasound associated with a specific faulting style?

In this paper, we use the University of Utah Seismograph Stations (UUSS) catalog of earthquakes from April 17, 2007 through June 30, 2012 ($M \geq 3.0$, N = 293) and nine infrasound arrays located in Utah to characterize epicentral infrasound. We use this dataset of infrasound detection to test the applicability of the MW05 relations to smaller earthquakes and to signals recorded at closer distances, including several within the 'zone of silence' (distances less than 220 km; Gutenberg, 1939).

CHAPTER 2

DATA

2.1 Earthquake Catalog

This study focuses on identifying infrasound generated from the epicentral region

of small earthquakes. We look for infrasound from all $M \geq 3$ earthquakes (total events =

293) in the UUSS catalog for the time period of April 17, 2007 (the install date of the

second Utah infrasound array) through June 30, 2012 (Figure 2.1; Table 2.1). Seismicity

in the Utah region predominantly occurs along the Intermountain Seismic Belt (ISB), a

zone of seismicity that extends from northern Arizona to northwestern Montana (Smith

and Arabasz, 1991). A notable exception was the 2008 $M_W5.9$ Wells, Nevada earthquake

and its subsequent aftershocks that occurred west of the ISB in the Basin and Range

province (labeled A in Figure 2.1). An important sequence occurring in the ISB is the

2011 $M_W4.5$ Tushar Mountains, Utah earthquake and aftershocks (labeled B in Figure

2.1).

2.2 Infrasound Data

Nine infrasound arrays are co-located with UUSS seismic stations (Figure 2.1).

These arrays are distributed both east and west of the ISB in order to maximize the

likelihood of recording epicentral infrasound. Three of the infrasound arrays (BGU, EPU,

and NOQ) were incorporated into the seismic network in 2006 and 2007 (Stump *et al.*,
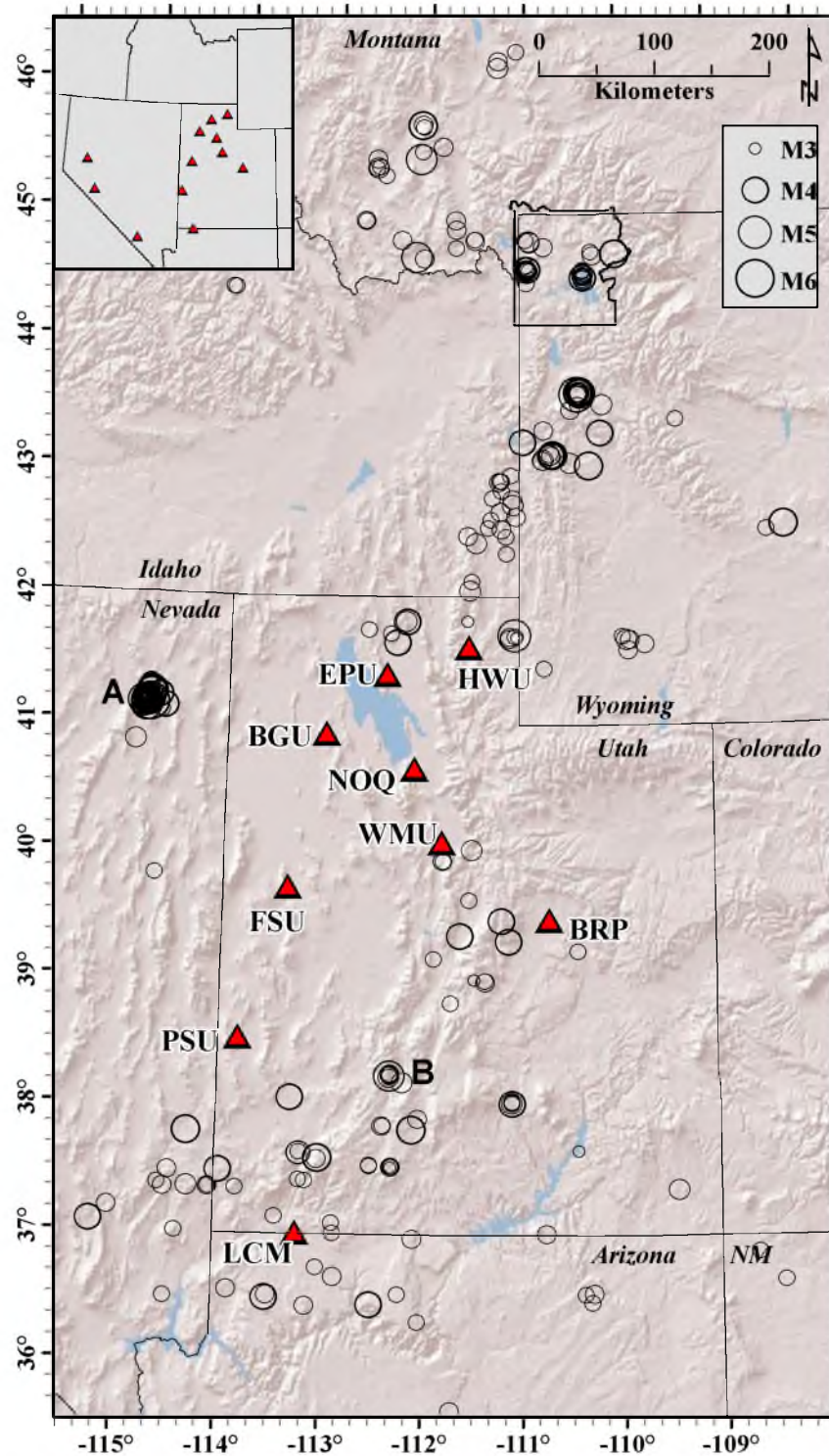
Figure 2.1. Map of infrasound arrays (labeled triangles) and the $M \geq 3.0$ earthquakes (circles, symbol sizes scaled by magnitude) from the UUSS catalog analyzed in this study. Labeled regions indicate the following significant earthquake sequences: A) Wells, NV 2008 and B) Tushar Mountains, UT 2011. Inset shows infrasound array locations including those in Nevada (north to south: FAL, NVAR, and DSR).

Table 2.1. Instrumentation

Array	Seismometer	Microphones	Telemetry	Install Date
BGU	Broadband Nanometrics Trillium 120	Chaparral 2	RADIO	17 April 2007
BRP	Broadband Nanometrics Trillium 240	Inter-Mountain Labs Model ST	CELL MODEM	16 April 2010
EPU	Short-period vertical Mark Products L-4C	Chaparral 2.5	RADIO	13 July 2007
FSU	Short-period Vertical Mark Products L-4C	Inter-Mountain Labs Model ST	RADIO TO A CELL MODEM	10 June 2010
HWU	Broadband Streckheisen STS-2	Inter-Mountain Labs Model ST	RADIO	14 May 2010
LCM	Broadband Guralp CMG-3T	Inter-Mountain Labs Model ST	RADIO OR CELL MODEM	11 September 2010
NOQ	Broadband Nanometrics Trillium 120	Chaparral 2	RADIO	4 May 2006
PSU	Broadband Nanometrics Trillium 120	Inter-Mountain Labs Model ST	RADIO OR CELL MODEM	12 September 2010
WMU	Short-period Vertical Mark Products L-4C	Inter-Mountain Labs Model ST	CELL MODEM	8 May 2010

See Appendix A for locations of each array element.

2007). Six new arrays (Figure 2.1 and Table 2.1) were installed between April and September 2010 for the purpose of this study.

Each of the infrasound arrays in Utah consists of four microphones arranged in a triangular configuration with one microphone in the center. The array aperture varies between roughly 100 – 150 m (Figure 2.2a). Array response analysis performed by Burlacu *et al.* (2010) shows that these arrays are best suited for detections at local to regional distances at frequencies between 1 – 5 Hz (Figure 2.2b). The arrays are equipped with Chaparral 2, Chaparral 2.5, or IML ST model microphones (Table 2.1). Within each array, the microphones are uniform. Laboratory tests confirm that the Chaparral 2 has a broader frequency response than the IML ST; however, the two sensors are flat within the 1 – 10 Hz band (Stump *et al.*, 2007). To dampen the effects of wind and local noise, each gauge is equipped with 8 – 10 inlet ports with attached 7.6 m long porous hoses creating rosettes. Data are continuously recorded and digitized at 100 samples-per-second on-site using REFTEK 130 or Quanterra Q330 dataloggers and then telemetered to the University of Utah in Salt Lake City where they are archived. The data are also available at the Incorporated Research Institutions for Seismology Data Management Center (http://www.iris.edu/dms/dmc/). For earthquakes where epicentral infrasound is detected, we obtained additional infrasound data from three arrays in Nevada (Figure 2.1, inset) through partnership with Southern Methodist University.
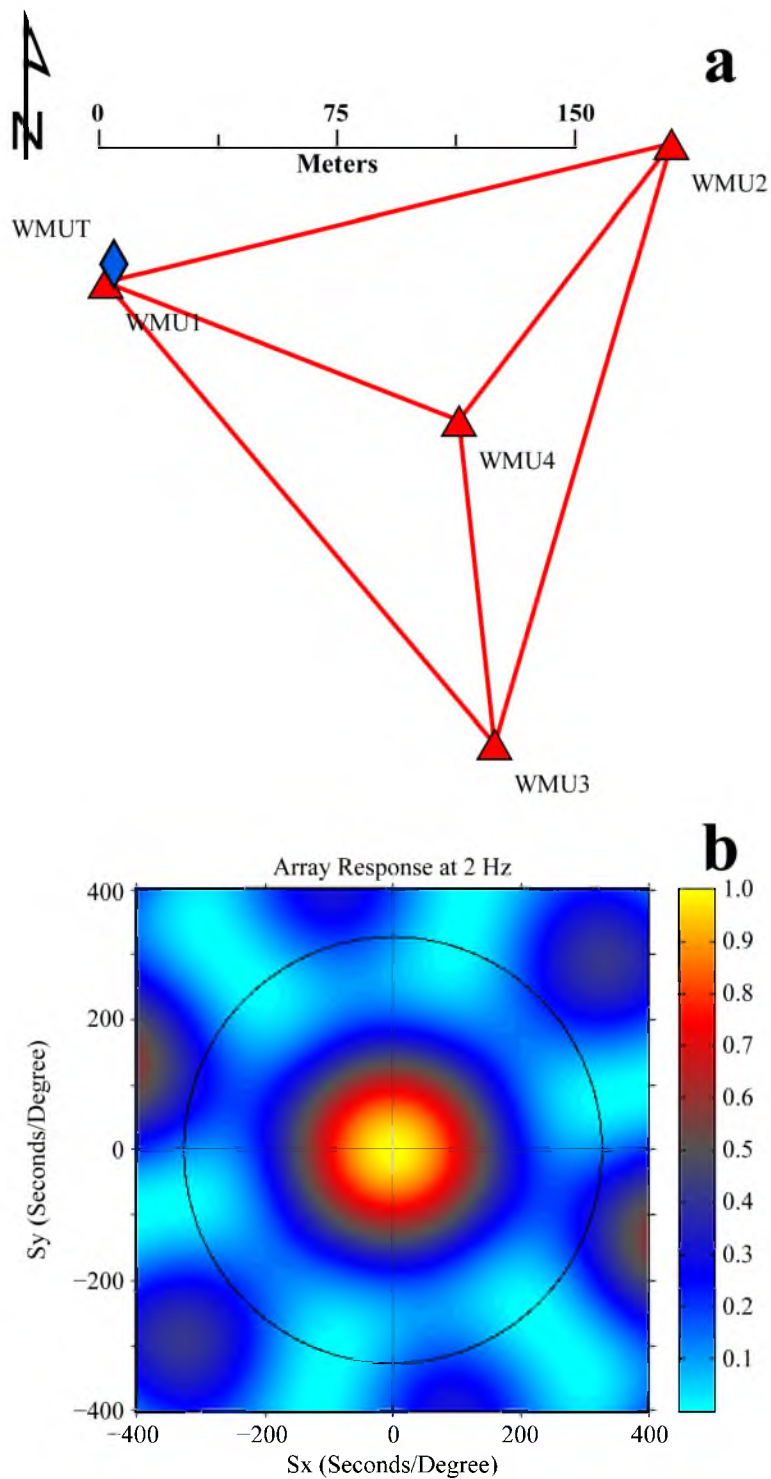
Figure 2.2. Example of a typical array layout and response. (a) Map view of infrasound array WMU. Microphone (triangles) spacing is approximately 100 m. The northwest element (WMU1) is co-located with a seismometer (diamond). (b) Normalized power (color scale) array response at 2 Hz in slowness space for WMU (Burlacu *et al.*, 2010). The black circle represents an apparent velocity of 0.34 km s^{-1}.

CHAPTER 3

INFRASOUND DATA PROCESSING

3.1 Preprocessing

For each earthquake in the catalog, infrasound data are retrieved from all available arrays beginning 45 minutes prior to the event origin time and ending 45 minutes after the expected arrival time for an epicentral thermospheric return assuming a 0.22 km s^{-1} group velocity. The data are filtered using a fourth-order Butterworth filter with corners at 1 and 5 Hz. To identify infrasound detections, filtered data are fed into the batch-processing feature of InfraMonitor 3.0 (Arrowsmith *et al.*, 2008).

InfraMonitor uses an adaptive noise hypothesis when correlating array components in order to account for time varying coherent noise sources. The long time window (45-minute buffers on both ends of the event window) is used to establish the coherent background noise level. To minimize the effects of correlated noise, we set the adaptive window to 7200 s. To optimize the noise hypothesis F-statistic, we set the P-value to 0.01 (Arrowsmith *et al.*, 2009).

3.2 Threshold Requirements for Establishing a Detection

We use a sliding-window (20-second time windows with 50% overlap) frequency-wave number analysis to obtain the backazimuth, F-statistic, correlation coefficient, and phase velocity for each discrete time window (Figure 3.1). In this study,
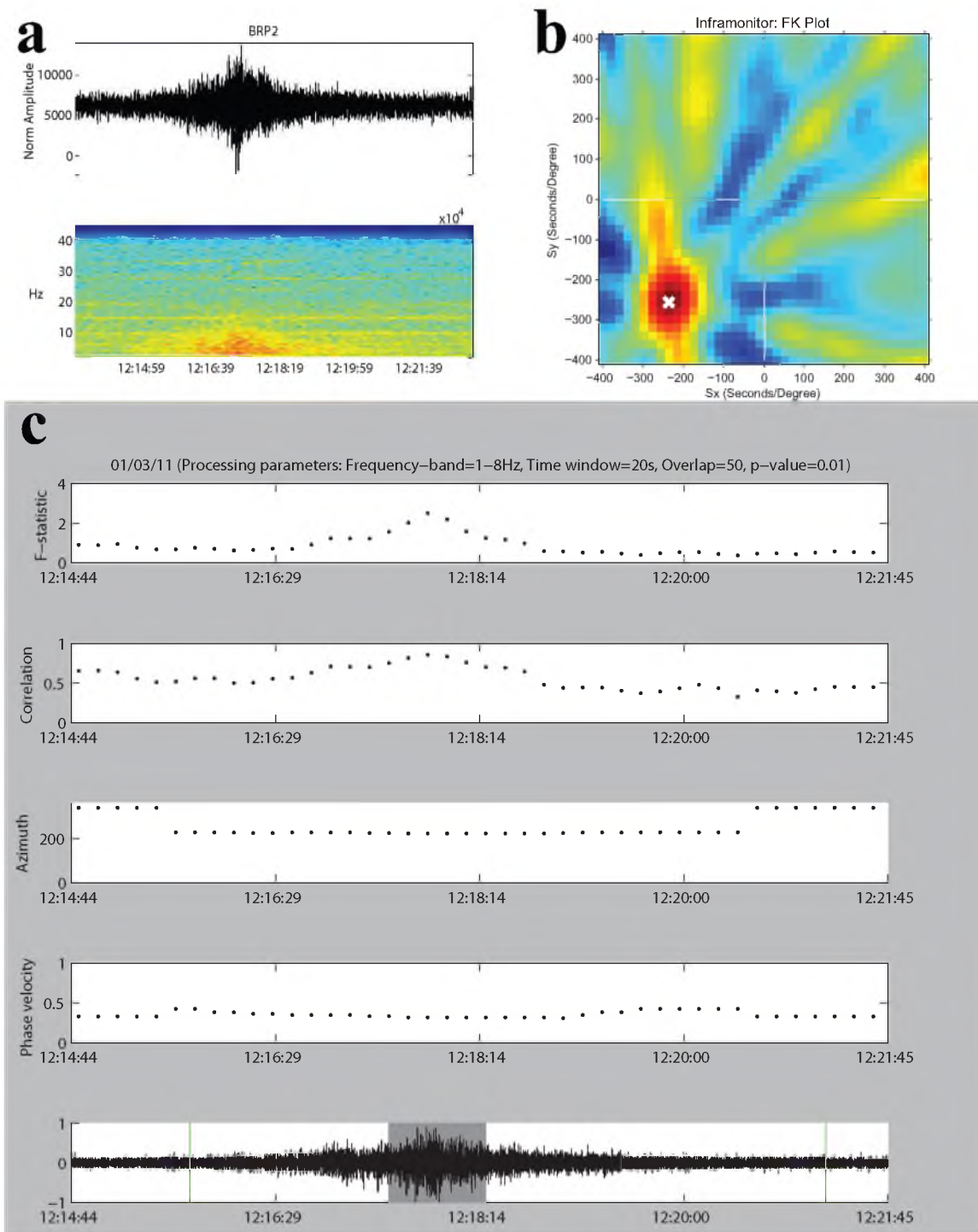
Figure 3.1. InfraMonitor GUI mode processing of a detection at array BRP from the 3 January 2011 M_L 4.6 Circleville, Utah earthquake (labeled B in Figure 2.1). (a) Raw trace of channel BRP2 (top) and spectrogram of the epicentral time window (bottom). (b) FK plot (seconds/degree) of the highest correlation window shown in (c). (c) Screenshot of the GUI showing the F-statistic, correlation, azimuth (°), phase velocity (km s^{-1}), and the BRP beam.

we focus on the travel-time window expected for epicentral infrasound defined by group velocities between 0.35 and 0.22 km s^{-1}. An epicentral infrasound detection is declared when the correlation coefficient is $\geq$ 0.5 and the azimuthal deviation from the direction to the epicenter, as reported in the UUSS earthquake catalog, is $\leq$ 8°. For completeness, detections with correlation coefficients $\geq$ 0.5 and azimuthal deviation between 8° and 20° are additionally reviewed.

To verify that the recorded signal was generated by the earthquake, we require detections at a minimum of two arrays and that the backazimuths must cross in the vicinity of the epicenter as reported by the UUSS earthquake catalog. Of the 293 earthquakes analyzed, 19 had epicentral time-window detections from two or more arrays. The detections from the 19 earthquakes are retained for further review. Detections consisting of a single 20 s discrete time window and detections with phase velocities $\geq$ 400 m s^{-1} are removed from the dataset as are detections consistent with other known infrasound sources such as ocean waves, surf infrasound, or internal gravity waves, generated by wind flow over orography (Arrowsmith *et al.*, 2010). After detailed analysis, 10 earthquakes had clear infrasound recordings from at least two of the arrays (Table 3.1).

3.3 Infrasound Detection Signal Measurements
3.3.1 Optimizing Infrasound Detection Data

In order to characterize the infrasound signal, the waveforms from the 10 earthquakes are prepared as follows:

Table 3.1 Epicentral infrasound detection characteristics.

No.	Origin	Latitude (°)	Longitude (°)	M_L	Depth (km)	Array	Dist. (km)	Amplitude Resp. Corr.Raw (Pa)	Distance Corrected (Pa)	Wind and Distance Corrected (Pa)	Duration (sec.)	Dominant Period (Hz)	Turning Altitude (km)	Turning Altitude Wind Velocity (m/s)
37	2008 02 21 14:16:02	41.1332	-114.8620	5.91	11	BGU	156							
						EPU	207	1.5030	0.1531	0.0578		1.3	44.0	23.5
						NOQ	237	1.7895	0.2219	0.0596		1.0	44.8	31.7
						NVIAR	421				201		109.1	6.0
38	2008 02 21 14:34:41	41.1495	-114.8680	4.51	11	BGU	157							
						EPU	208	0.3566	0.0366	0.0137	245	2.0	43.9	23.7
						NOQ	238	0.2256	0.0281	0.0076	248	1.7	44.8	31.7
68	2008 02 22 01:50:05	41.1282	-114.8740	4.03	11	BGU	157	0.1000	0.0068	0.0017	239	5.7	42.3	33.9
						NOQ	238	0.0559	0.0070	0.0016		1.7	45.5	35.5
83	2008 02 22 23:24:03	41.1078	-114.9150	3.55	8	BGU	160	0.0447	0.0031	0.0009	89	3.7	39.5	29.2
						EPU	212							
						NOQ	241	0.1081	0.0137	0.0063		1.7	37.7	18.9
84	2008 02 22 23:27:45	41.1055	-114.9000	4.48	12	BGU	159	0.3532	0.0245	0.0072	220	3.3	39.4	29.4
						EPU	211	0.0720	0.0075	0.0011		2.7	44.7	46.3
						NOQ	240	0.1755	0.0222	0.0051		1.3	45.4	35.5
110	2008 04 01 13:16:17	41.2257	-114.8440	4.54	12	BGU	156	0.0632	0.0043			1.3	0.8	1.6
						EPU	205	0.0525	0.0053		287	4.4	2.0	18.4
150	2009 01 16 04:15:34	43.2138	-111.0130	4.08	8	*BGU*	*304*							
						EPU	233	0.0486	0.0059	0.0017	97	2.0	37.0	30.5
219	*2010 08 05 14:59:27*	*43.5978*	*-110.4140*	*4.31*	*9*	*HWU*	*240*							
						WMU	*408*	*0.1783*	*0.0486*		*14*	*5.7*	*104.7*	*33.2*
243	2011 01 03 12:06:36	38.2473	-112.3400	4.56	5	BGU	303	0.0202	0.0036		398	1.7	107.2	64.7
						BRP	194	0.1366	0.0127	0.0032	315	2.0	37.8	33.1
						EPU	349	0.0280	0.0061	0.0036	361	4.0	53.0	12.9
						HWU	379	0.0218	0.0053		506	1.7	106.5	63.4
						WMU	208	0.0721	0.0074	0.0025	482	1.3	42.2	25.8
255	2011 04 05 07:05:24	44.6630	-112.1650	4.57	11	HWU	343	0.0245	0.0052	0.0031	93	2.0	44.8	12.8
						PSU	695							

Italicized values are not used in results analysis.

- The instrument response for each sensor is removed through deconvolution in the frequency domain with corners at 0.5 and 10 Hz. These corners are outside the expected coherent epicentral infrasound frequencies for the events of interest.

- The spectrogram for each response-corrected epicentral time window is reviewed in order to optimize the bandpass filter to be used during array processing. For example, based on the spectrogram in Figure 3.1a, the data would be filtered from 1 – 8 Hz. In cases where there is no clear peak in the signal, the data are filtered using the same 1 – 5 Hz corners used during batch processing.

- The response-corrected filtered data are array-processed using the same techniques and parameters used during batch processing.

- The optimized beam is calculated using the backazimuth and phase velocity corresponding to the highest correlation window. The fk plot (slowness in seconds-per-degree; Figure 3.1b) from the highest correlation window (Figure 3.1c) is reviewed to assess the quality of the detection. The beam is displayed along with phase velocity, azimuth, correlation, and F-statistic values for each discrete time window for quality assessment (Figure 3.1c).

3.3.2 Measuring Amplitude and Duration

Using the beam, we measure the duration, amplitude, and dominant frequency for each of the detections. In certain cases, it is not possible to make accurate measurements due to poor signal-to-noise ratios or because the presence of secondary infrasound and seismic phases from aftershocks interfere with the primary infrasound detection. Duration measurements (Figure 3.2a; Table 3.1) are calculated by applying an envelope function (equation 3.1) to the beam, where x_n is the original beam and y_n is its Hilbert transform.
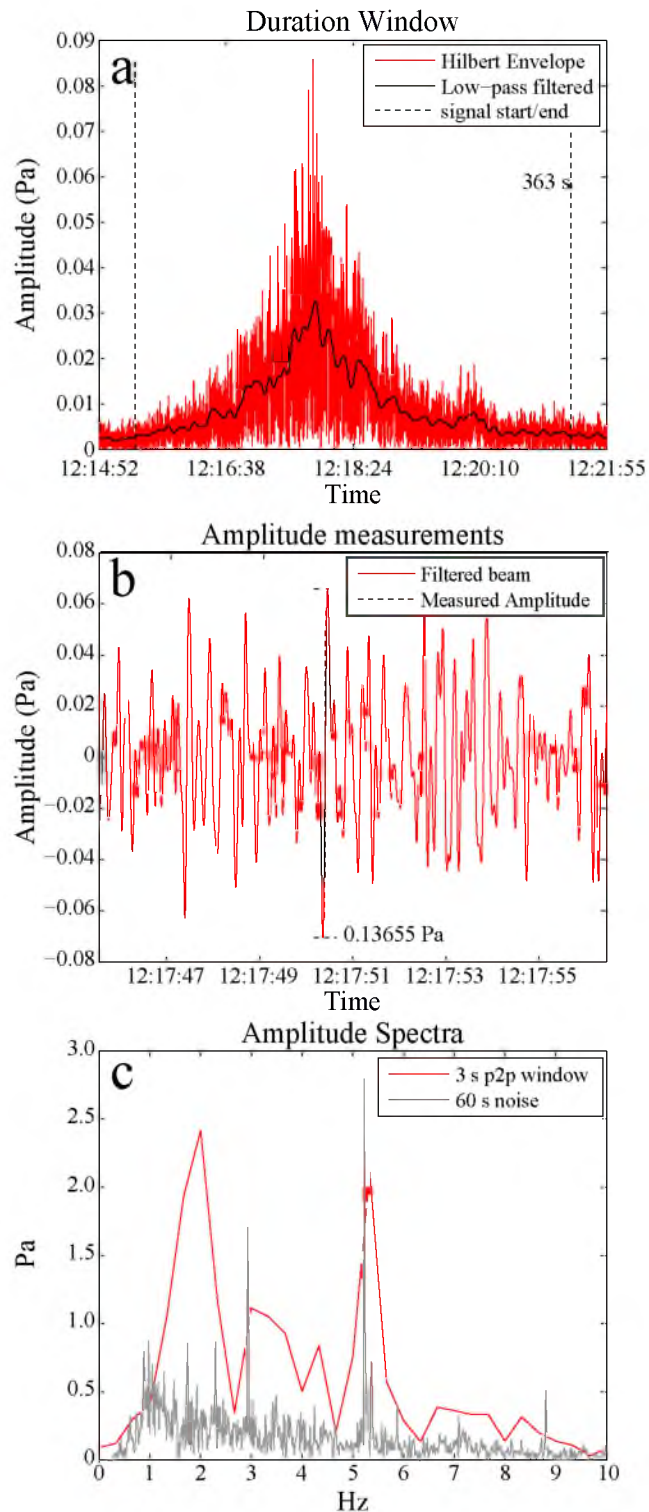
Figure 3.2. Example of infrasound measurements used in this study. (a) Envelope of the beam and the 8 s low-pass of the envelope are used to determine duration (363 s). (b) Maximum peak-to-peak amplitude measurement of the beam in Pascals (0.13655 Pa). (c) Amplitude spectra of the beam taken at the maximum amplitude of the detection and during pre-event noise.

$$|H_b| = \sqrt{(x_n{}^2 + y_n{}^2)} \qquad (3.1)$$

The start and end times of the duration are defined where the eight-second low-pass envelope function continually exceeds the background noise levels (Figure 3.2; Table 3.1).

To estimate the amplitude, we measure the maximum peak-to-peak amplitude within the detection window (Figure 3.2b; Table 3.1). In the case where two separate events are close enough in time that detections from each occur in overlapping epicentral time windows, the detections and measurements are attributed to the event based on group velocity and event order.

To estimate the dominant frequency of the detection, we evaluate the amplitude spectrum for 3 s centered at the time of the peak-to-peak amplitude including half-second tapers on either side. This spectrum is compared to that of 60 s pre-event noise, including 10 s tapers on either end (Figure 3.2c; Table 3.1).

3.4 Removal of Detection

The WMU detection for earthquake #219 fits our criteria and is included in Table 3.1. However, the duration is three orders of magnitude smaller than the predicted value, using MW05 relations. Typically, a signal with a short duration should also have a small amplitude. For the WMU detection, the amplitude is nearly double the MW05 predicted value. In addition, the peak frequency is 5.7 Hz, which is high for a detection past 400 km. The next closest observation (379 km) has a frequency of 1.7 Hz. Due to these inconsistent measurements, this detection is not included in the statistics and regressions discussed in Chapter 5.

CHAPTER 4

RAY TRACING

4.1 Calculating Ray Paths

Three variables affect acoustic amplitude observations: temperature, wind speed, and wind direction, all three of which can vary with time, azimuth, and altitude. For the ten earthquakes with two or more detections, the atmospheric profile model from ground-to-space (G2S, Drob *et al.*, 2003) is calculated for the epicenters and hours closest to the earthquake origin time. TauP2.1 (Arrowsmith, 2012b) is used to ray-trace through each G2S atmospheric model from the epicenter (elevations taken from Google Earth) to the center of the infrasound array. Ray paths are computed for every 1° in azimuth and 2° in launch angle. Rays within 50 km of the station are further evaluated in TauP2.1 to find the ray path with the bounce point closest to the receiver. This ray is selected as the preferred path. The preferred path is used to determine the distance error between the closest ray bounce point and the center of the array, predicted group velocity, predicted azimuth, turning altitude, and the wind velocity (m s^{-1}) at the turning altitude.

For each source-receiver path with a unique atmospheric profile there are often multiple ray paths. A special case exists when the atmospheric profile, at the time and location of an earthquake predicts bounce points near the receiver from rays turning in the troposphere, stratosphere, and thermosphere. In this special case, the preferred ray path is chosen based on comparison between the observed and predicted group velocities.

For example, for earthquake #243 (Table 3.1) the G2S profile directed towards the array at HWU predicts turning rays at five different altitudes: (a) 44.5 km, (b) 57 km, (c) 61.5 km, (d) 106.5 km, and (e) 122.5 km (labeled in Figure 4.1). Rays turning at both 61.5 km and 106.5 km reach HWU. The observed group velocity for the detection at HWU is 0.263 km s^{-1}, which most closely matches the predicted group velocity of 0.269 km s^{-1} for the ray turning at 106.5 km.

4.2 Ray Tracing Errors and Exceptions

For two detections (HWU, earthquake #255 and EPU, earthquake #150, Table 3.1), the G2S profiles do not predict bounce points within 50 km of the station, although the detections clearly meet the criteria for correlation, group velocity, and azimuthal deviation. To identify the preferred path, we evaluate the G2S temperature and wind profiles (Figure 4.2). In each case, the effective sound speed predicted at stratospheric elevations approaches the effective sound speed at ground levels. Differences in the effective sound speeds at these two elevations are only 0.6 and 2.8 m s^{-1}, respectively. These values are well within the stated geophysical uncertainty for the global numerical weather prediction at the stratopause of 5 m s^{-1} (Arrowsmith *et al.*, 2010). Given the uncertainties in predicted wind speeds, we use the turning altitudes where the atmospheric sound speeds are closest to the predicted ground level sound speeds to determine the preferred atmospheric ray path.
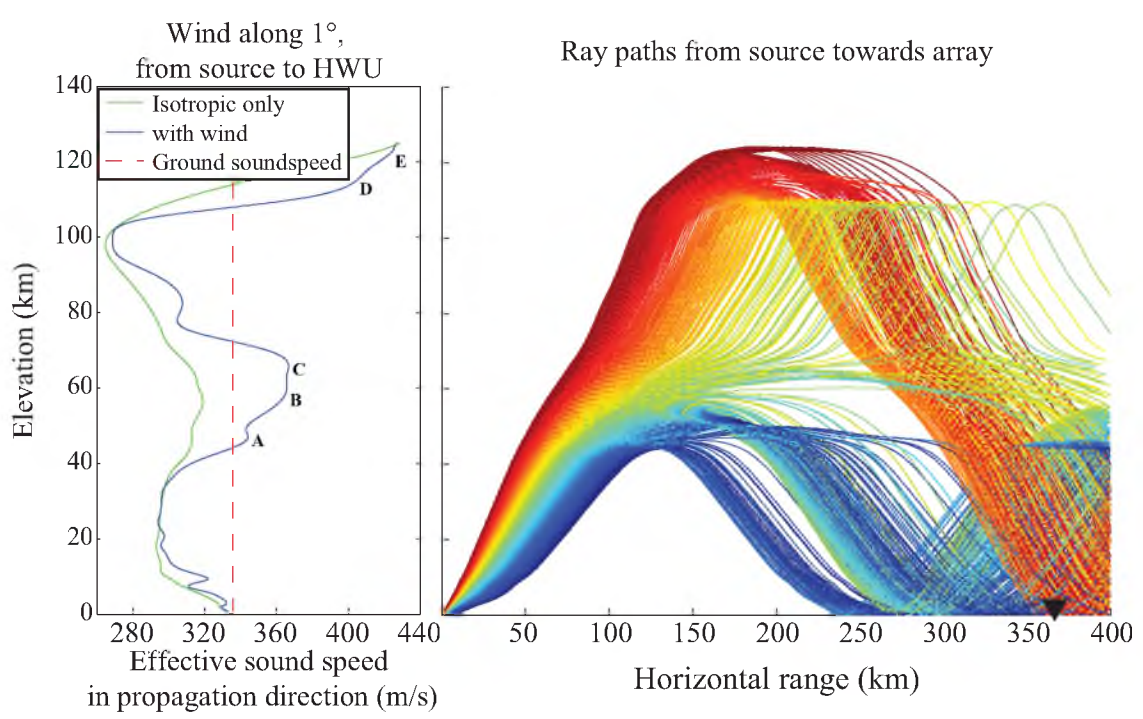
Figure 4.1. Ray tracing through a complex atmospheric profile. Left: G2S profile for time of earthquake #243 (Table 3.1 and Appendix B) directed towards array HWU. Letters denote altitudes and wind speeds where ray paths turn (shown at right). Right: Predicted infrasound ray paths (lines colored from low-angle, blue to high-angles, red) for the G2S profile (left) radiating from the event (origin) to the array (black triangle).
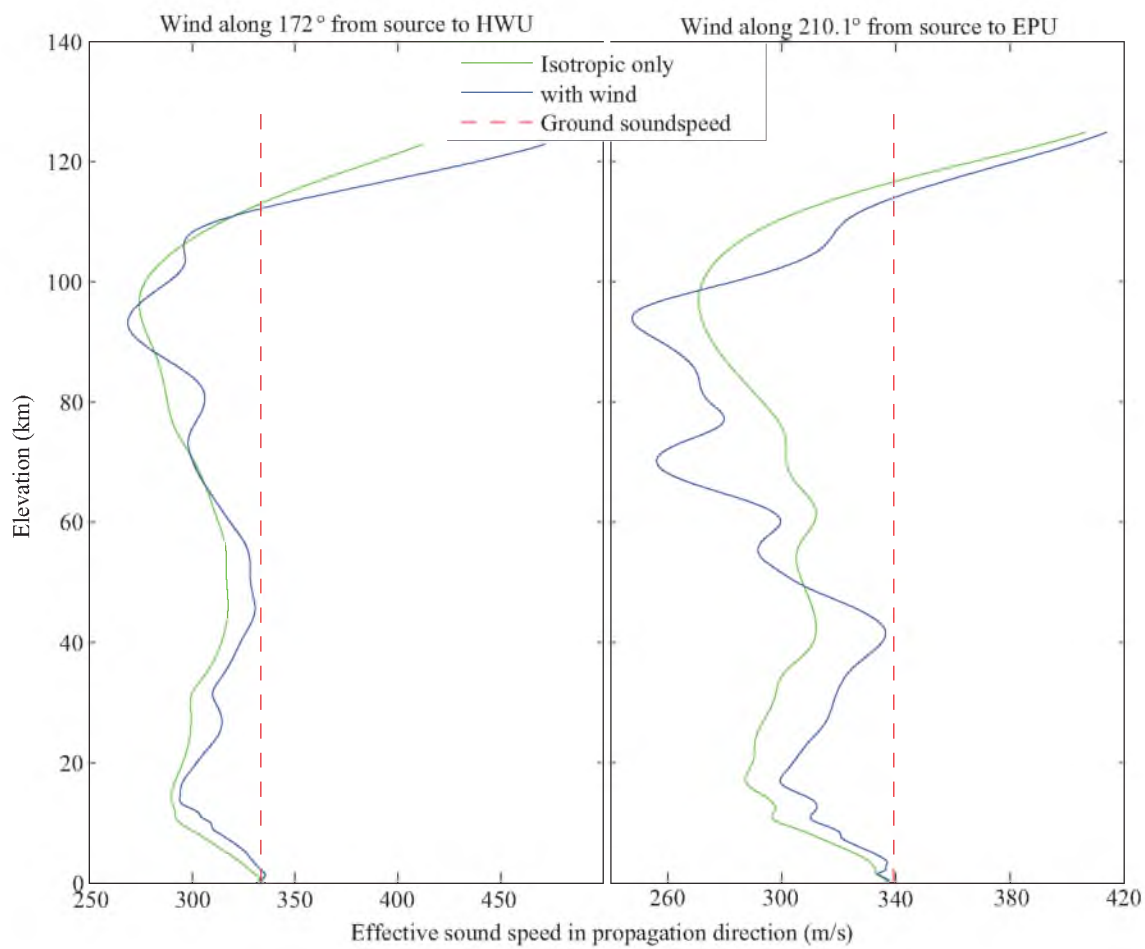
Figure 4.2. G2S profiles for earthquakes #255 (left) and for #150 (right) in Table 3.1 and Appendix B.

CHAPTER 5

MUTSCHLECNER AND WHITAKER (MW05) RELATIONS

MW05 used epicentral infrasound observations from 31 earthquakes ($4.4 \leq M_L \leq 7.5$) during 1983 – 2003 to identify scaling relationships between seismic magnitude and either the log of epicentral infrasound amplitude (corrected for stratospheric winds and normalized for distance) or the log of signal duration. For each case, they found that linear relations exist. MW05 additionally proposed that a minimum peak surface acceleration threshold between 10 and 20 cm s^{-2} exists for atmospheric infrasound generation.

Our dataset from 2007 – 2012 has observations for smaller magnitude earthquakes $3.55 \leq M_L \leq 5.91$ recorded at closer distances (156 – 695 km). This dataset is used to test the applicability of the MW05 relations to smaller earthquakes.

5.1 Durations

The MW05 relation for duration versus earthquake magnitude is a direct comparison between the log of the observed signal duration (minutes) and the magnitude of the earthquake. MW05 concluded that the extent of the epicentral area with ground motions that exceed the threshold for infrasound generation is proportional to the observed signal duration.

5.2 Amplitude Corrections

Following MW05, the response corrected infrasound amplitudes A_o are normalized for the effects of distance and wind using the following equation:

$$A_n = A_o 10^{-kV_d} \left(\frac{R}{R_s}\right)^s \qquad (5.1)$$

where A_n is the normalized amplitude, R is the great circle distance between station and epicenter, R_s is a normalized distance, here 1000 km (Mutschlecner and Whitaker, 2005), and V_d is the stratospheric wind component directed from source to infrasound array determined from ray tracing; s and k are empirical parameters determined in Mutschlecner *et al.* (1999), $s = 1.45$ and $k = 0.018$ s m^{-1}. Measurements for raw, distance corrected, and, when appropriate, distance-and-wind corrected amplitudes are listed in Table 3.1. It is important to note that equation 5.1 is applicable to stratospheric turning rays only (Mutschlecner *et al.*, 1999). For tropospheric and thermospheric returns, the amplitudes are corrected for distance only by setting V_d to zero in equation 5.1. For stratospheric returns, V_d is the average wind speed (m s^{-1}) predicted by G2S over 1 km centered at the turning altitude of the preferred raypath. This differs from MW05 which used an average wind speed between 45 – 55 km altitudes derived from atmospheric profiles interpolated between rocketsonde data collected on nearby calendar days.

5.3 Peak Ground Motion

MW05 proposed that a minimum peak ground acceleration (PGA) of 10 – 20 cm s^{-2} is required to generate epicentral infrasound. To explore this suggestion, we calculate predicted PGA values for earthquakes in our catalog, for $3.0 \leq M < 5.0$ using Chiou *et al.*

(2010), and for $M \geq 5.0$ the Chiou and Youngs (2008) relations. Pankow (2012) compared PGA measurements on broadband and strong motion instruments from 163 Utah earthquakes ($3.0 \leq M_L < 5.5$) to various ground motion prediction equations for small-to-moderate earthquakes and showed that Chiou *et al.* (2010) best fit the Utah data.

The key input to the predicted ground motion calculations is the average shear-wave velocity to a depth of 30 m (Vs30) at the local site. For epicenters occurring in the Utah region, we use Vs30 values from McDonald and Ashland (2008) (see Pankow, 2012 for greater detail). For earthquakes outside of the Utah region, we rely on the Global Vs30 Map Server (http://earthquake.usgs.gov/hazards/apps/vs30/). The USGS Vs30 values were derived by correlating Vs30 measurements against topographic slope as a proxy for Vs30 values in active tectonic regions (Allen and Wald, 2009). For both datasets, we treat Vs30 values ≥ 700 m s^{-1} as rock sites and assume 1 km of Quaternary sediment overlying bedrock for all other sites.

CHAPTER 6

RESULTS

6.1 Detection Catalog Characteristics

All earthquakes analyzed in this study are assigned event IDs in chronological

order (Appendix B). The ID numbers in Table 3.1 correspond to earthquakes listed in

Appendix B. Table 3.1 contains the epicentral infrasound detection and all associated

observational data. We investigate earthquake sources because normal-faulting

earthquakes are known to generate infrasound while strike-slip earthquakes are not

known sources (ReVelle *et al.*, 2004). Both source types occur in the catalog region. The

M_W and corresponding focal mechanism (when available from Whidden and Pankow,

2012 or Hermann *et al.*, 2011) of earthquakes with multiple detections are shown in

Figure 6.1 and listed in Appendix B. We see observations from earthquakes with focal

mechanisms ranging from normal (five) to oblique-normal (two) to strike-slip (one). We

were unable to identify a focal mechanism for one earthquake (#83). The amplitude of

the measured detection (HWU) from the M4.6 Dillon, MT strike-slip earthquake (#255)

agrees well with the M4.6 Tushar Mountain, UT detection at similar distance (EPU). The

durations have significant differences possibly related to mechanism.

In this study, infrasound detections are observed at smaller magnitudes than

previously documented by MW05. We identify multiple infrasound detections in the

magnitude range $3.55 \leq M \leq 5.91$, including measurements from three earthquakes
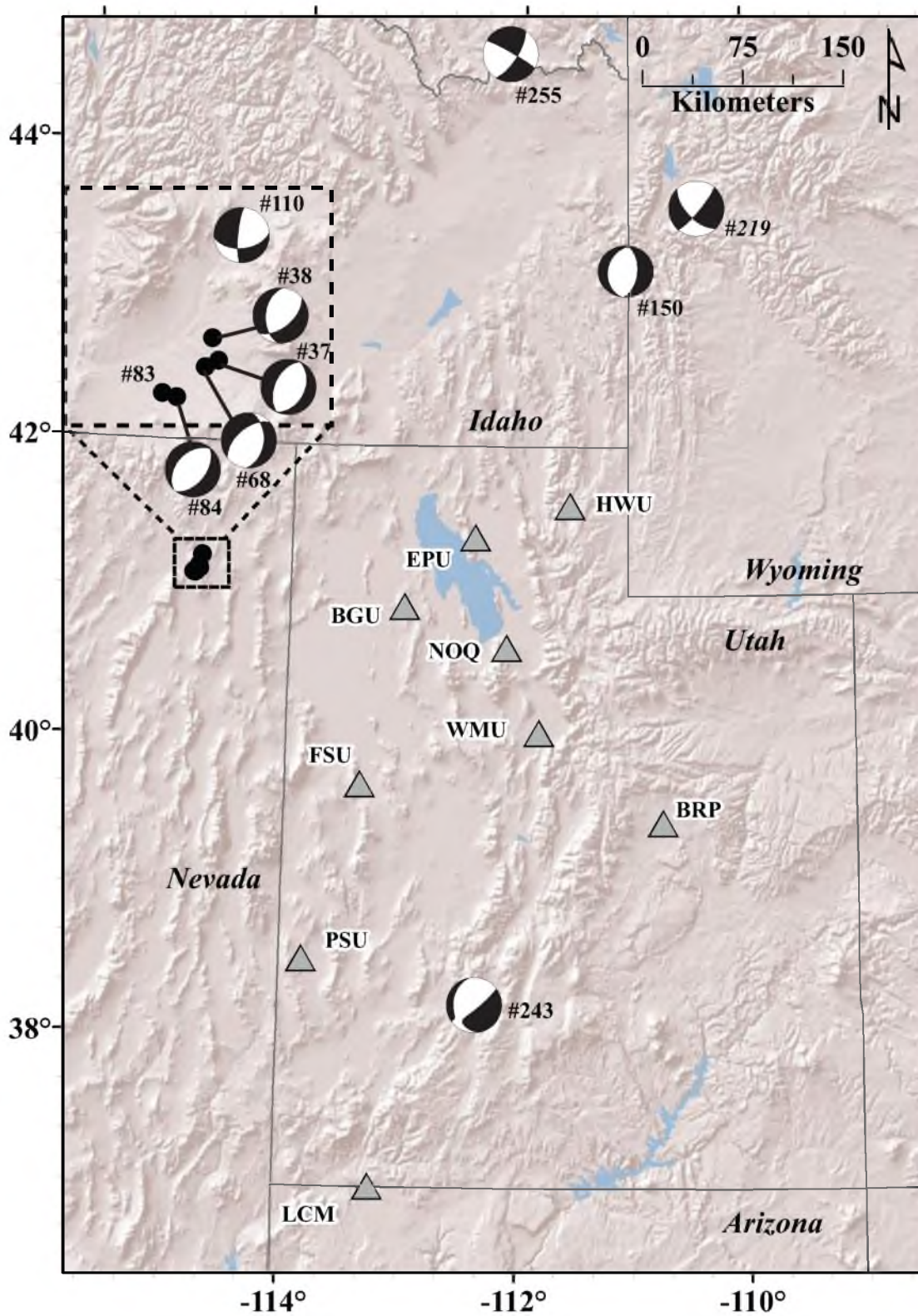
Figure 6.1. Map of earthquakes (numbers correspond to Table 3.1) with infrasound detections (black circles and/or focal mechanisms when available). Triangles show the location of infrasound arrays.

below the MW05 minimum of M_L4.4. MW05 states that they detected aftershocks from the Northridge earthquake down to $M_L = 3.5$, though these detections were not included in their paper. We also detected infrasound within the 'zone of silence' (distances < 250 km). These new infrasound observations at small magnitudes, close distances and for events with differing mechanisms show that infrasound is generated for a wider magnitude range and faulting styles than in previous studies.

Signal durations of the observed earthquakes range from 89 s to close to 9 minutes (Figure 6.2a). We observe peak frequencies from 1 – 5.7 Hz (Figure 6.2b). The 1 Hz minimum corresponds to the low-pass used for several events. Our maximum azimuthal deviation between the observed backazimuth at the maximum correlation and the backazimuth to the epicenter is ±20° for allowed detections and ±8° for measured detections. All but one detection falls into the higher quality azimuthal deviation category (Figure 6.2c).

We did not detect epicentral infrasound from all earthquakes analyzed, for which there are two main possibilities: 1) the arrays were not optimally oriented for the seismicity or 2) some threshold for infrasound generation was not met.

6.2 Seasonal Variations of Stratospheric Winds

We categorize our results as summer or winter detections to account for the change in stratospheric wind directions that occur seasonally. The stratospheric flow is predominantly zonal and reverses directions, moving eastward in the winter and westward in the summer. During equinox, the stratospheric winds are much lighter. This change in wind direction affects our detection probabilities and sampling. For simplicity, we use the vernal and autumnal equinoxes to delineate the start and end of summer,
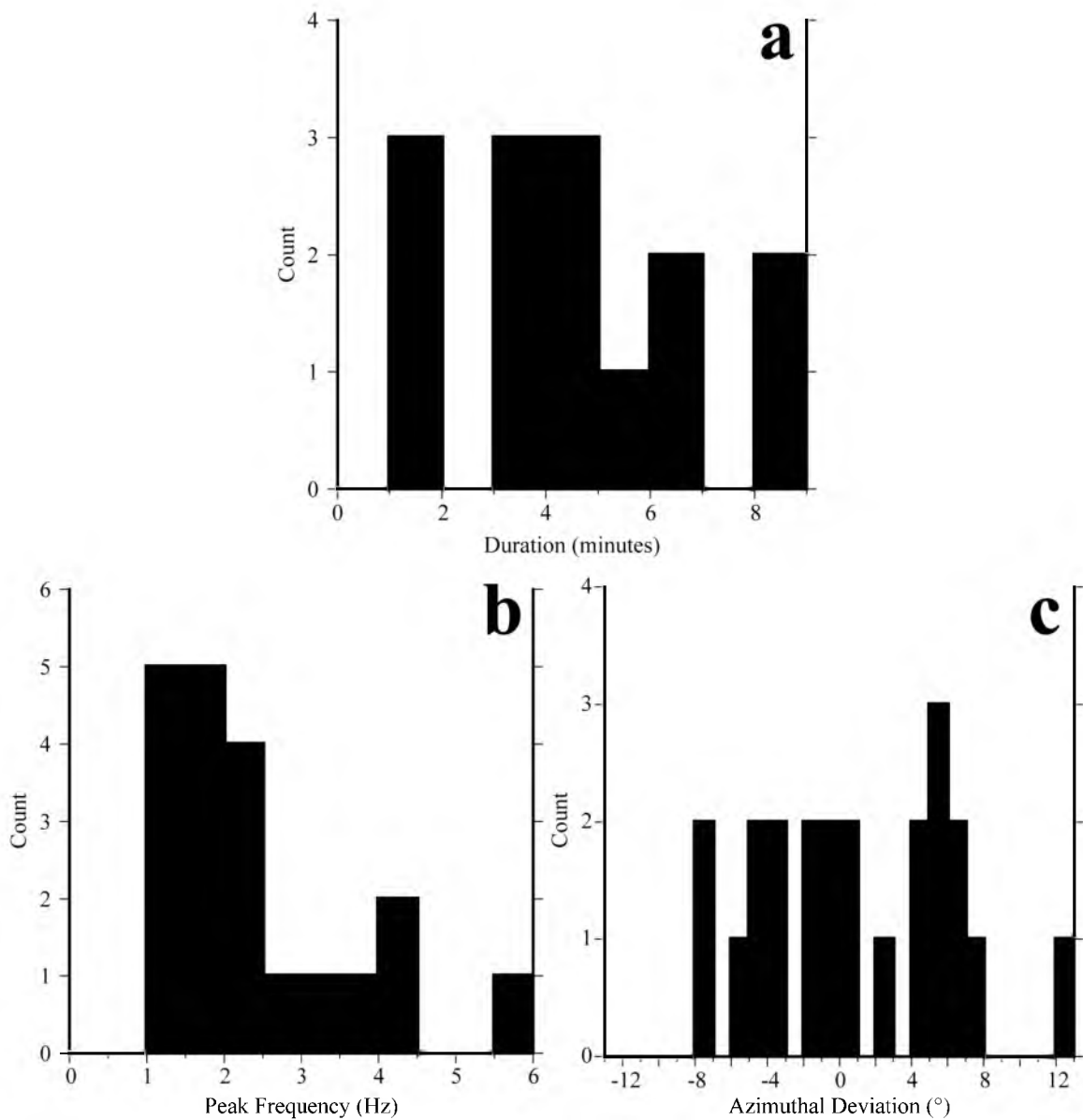
Figure 6.2. Histograms of detection characteristics for (a) duration in 1-minute bins, (b) peak frequency in 0.5 Hz bins, and (c) deviation between great-circle path backazimuth and the backazimuth returned during array-processing in one degree bins.

respectively. Atmospheric conditions are more favorable for detecting infrasound during winter due to the strong stratospheric ducting (Drob *et al.*, 2003). For detections recorded during the summer, ray-tracing only predicted one stratospheric return.

The data distribution of magnitudes for summer versus winter detections is skewed by the Wells, NV earthquake sequence (Figure 6.3a, red), which is responsible for 17 detections from six earthquakes, including one during summer (Figure 6.3). The Wells, NV *M*5.9 mainshock generated 75 aftershocks located by UUSS, which dominate the winter distribution and are the main cause of the discrepancy in the number of winter and summer earthquakes (Figure 6.3). Azimuthal distribution for the total possible detections from the epicenter to the array (Figure 6.3b) shows good symmetry between summer and winter when the Wells, NV events (red) are ignored. This symmetry is not reflected in the detections where there are only two non-Wells-related detections from one earthquake in the summer time (near 180°); the winter detections are moderately spaced in azimuth.

We also look at the proposed MW05 threshold for generating infrasound, 10 – 20 cm s^{-2}. Earthquakes below this threshold (Figure 6.4, gray bars) are unlikely to generate infrasound. This holds true here as all the detected earthquakes have PGA values above 10 cm s^{-2} (Figure 6.4, inset). There are 205 earthquakes with a predicted PGA $\geq$ 10 cm s^{-2} and 83 of those have PGA $\geq$ 20 cm s^{-2}, yet only nine generated infrasound detections. For PGA (Figure 6.4), we see a similar distribution between seasons, including one earthquake for each season above 240 cm s^{-2}. These are the Wells, NV *M$_W$5.9* earthquake, which produced observed infrasound to the east during winter, and the Grovont Peak, WY *M$_L$5.2* earthquake, which did not generate infrasound observations to the southwest
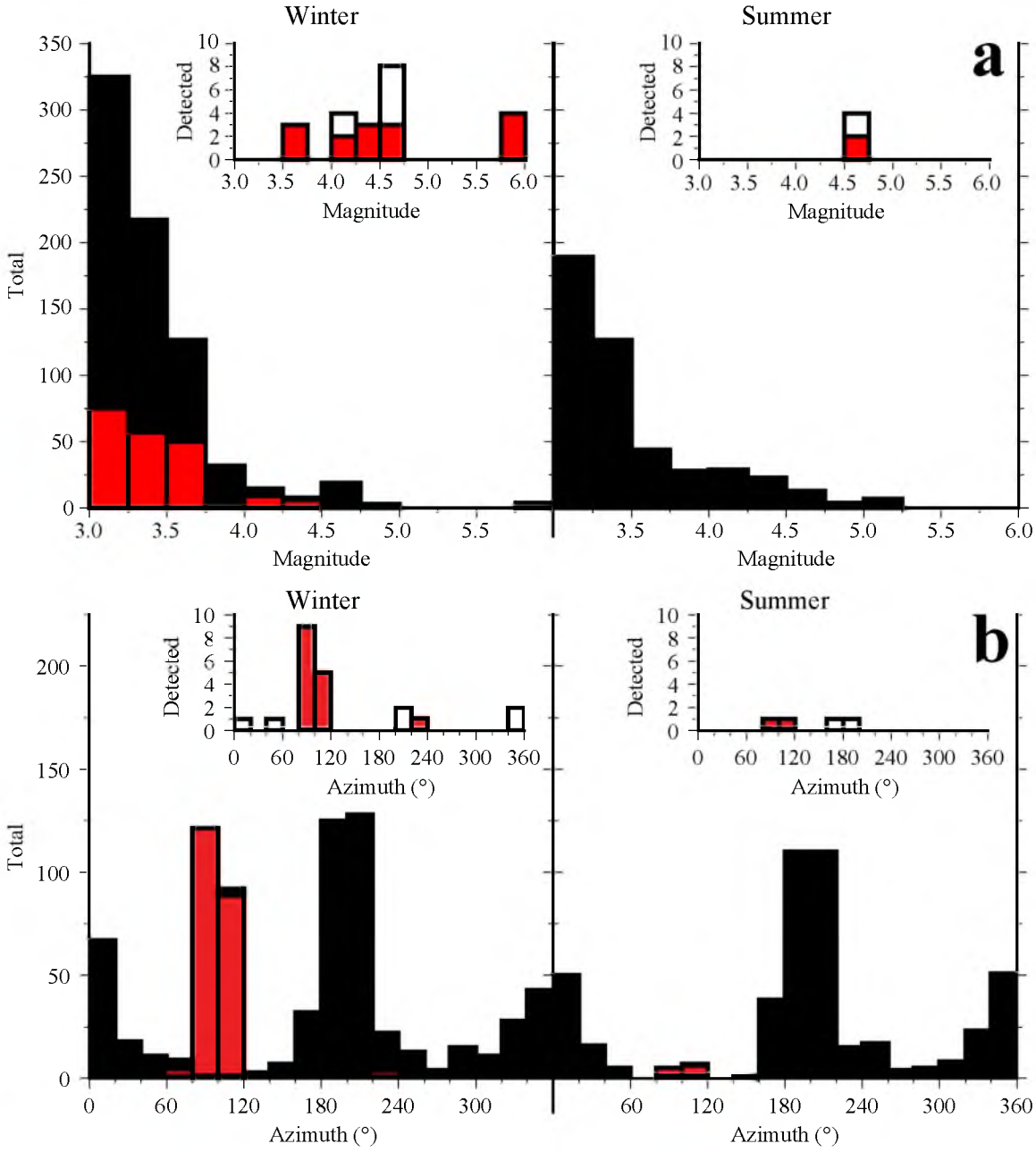
Figure 6.3. Magnitude (a) and azimuth (b) histograms for the full catalog (main) and detections (inset) separated into summer and winter periods divided on the vernal and autumnal equinoxes. Red bars identify number of contributions from the Wells, NV sequence.
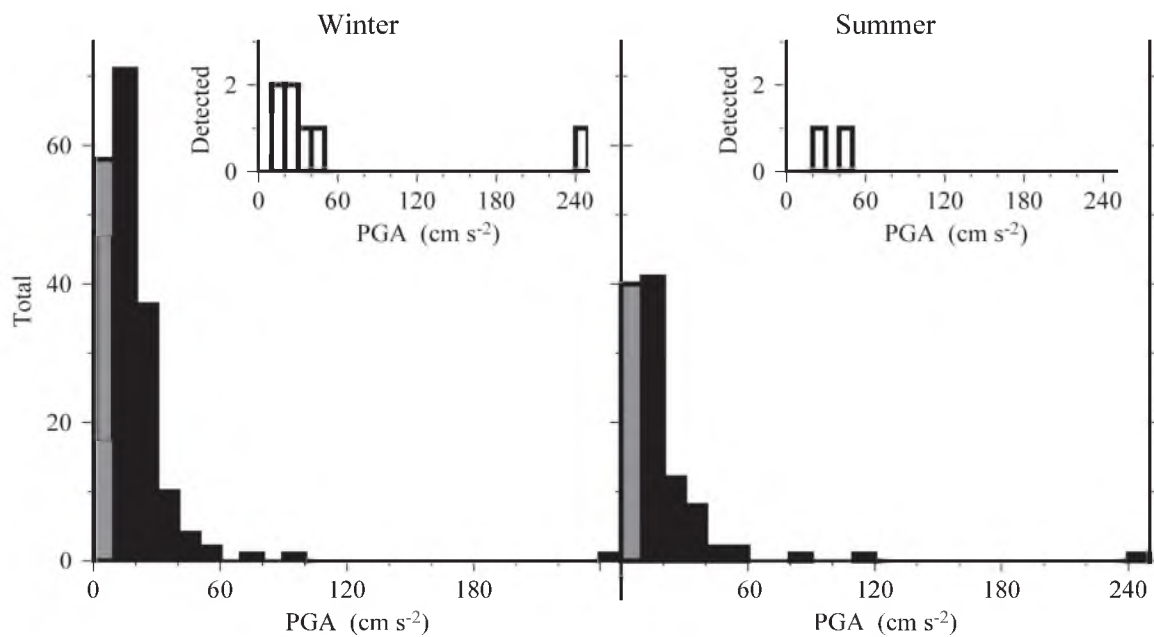
Figure 6.4. Peak ground acceleration histograms for the full catalog (main) and detections (inset) separated into summer and winter periods divided on the vernal and autumnal equinoxes. Full catalog shows earthquakes not expected to generate infrasound according to MW05 (gray) and events that are above the threshold of $10 - 20$ cm s^{-2} (black).

during summer. However, it is one of the largest earthquakes and generated

approximately the same PGA as the Wells, NV M_W5.9 earthquake.

6.3 Amplitude-Magnitude Relation

MW05 first identified a least squares fit between the normalized amplitudes,

log(A_n) and M_L (Figure 6.5, solid black). Their least squares relation is

$$\log(A_n) = 0.55M_L - 4.01 \qquad (6.1)$$

This relation is for the best-determined stratospheric detections though there were only

slight differences between the detections listed in MW05 and their more inclusive data

set. We also compared stratospheric data that had been wind and distance corrected to a

mix of returns from all atmospheric layers and noticed only subtle differences. To be

consistent with MW05, we omit the nonstratospheric detections (Figure 6.5, gray circles)

in our least squares fit for the stratospheric data (black circles). Our data show similar

scatter to MW05. When the data from both studies are combined, the linear fit (blue line)

$$\log(A_n) = 0.51M_L - 3.74 \qquad (6.2)$$

shows no significant improvement in fit. The standard deviations for regressions of

MW05 and this study are 0.404 and 0.402, respectively.

6.4 Duration-Magnitude Relation

Figure 6.6 shows the relations between magnitude and duration. Much like the

magnitude-amplitude relations, these also show a correlated fit, though the scatter is

significant. The MW05 least squares fit is
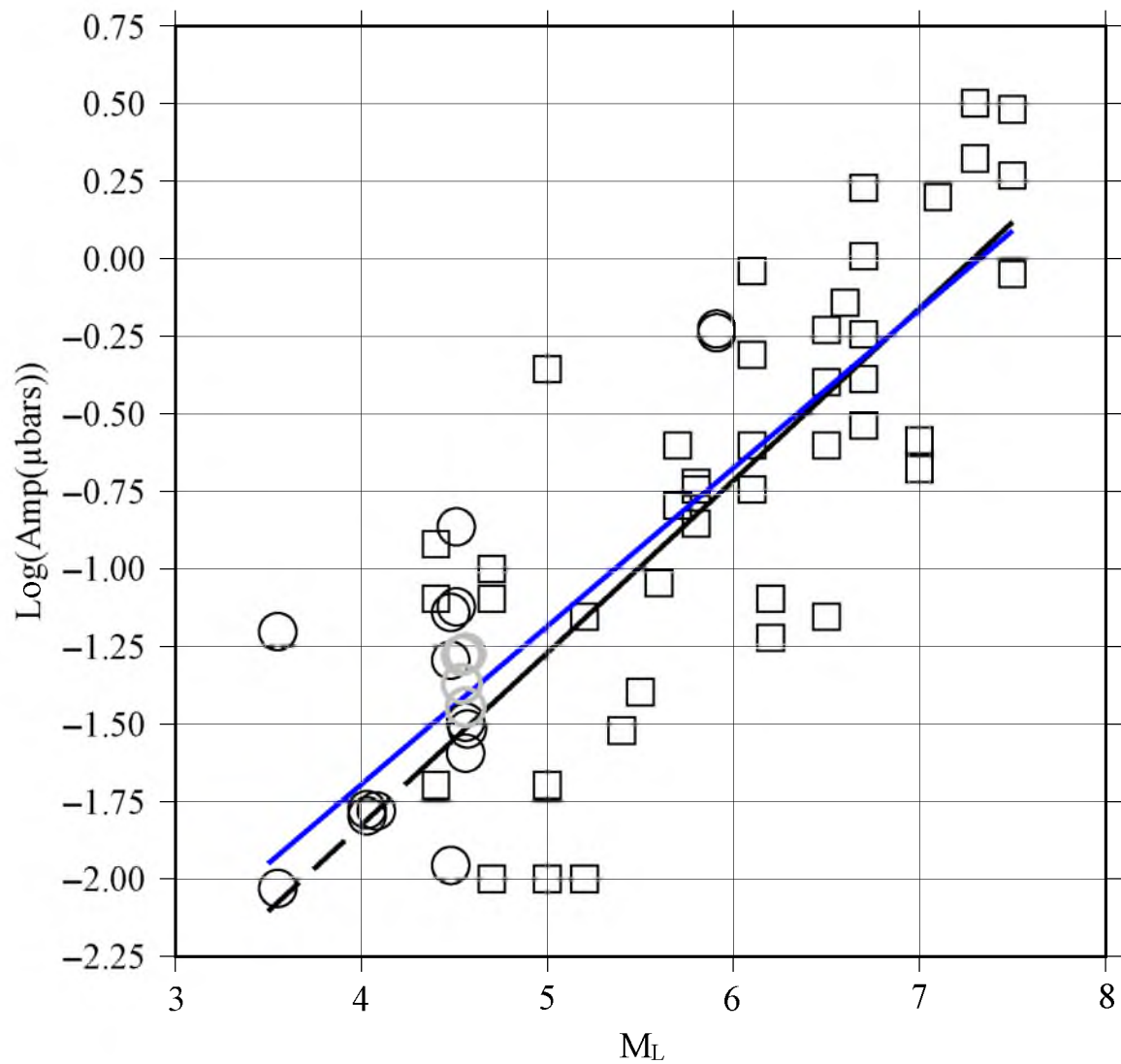
Figure 6.5. Log of peak amplitudes normalized for distance and wind effects (black symbols) versus magnitude. MW05 detections (squares) and the MW05 regression line (black, dashed black is the projection to $M3.5$). Detections identified in this study (circles) nonstratospheric detections (gray circles). Regression for the combined datasets (blue line).
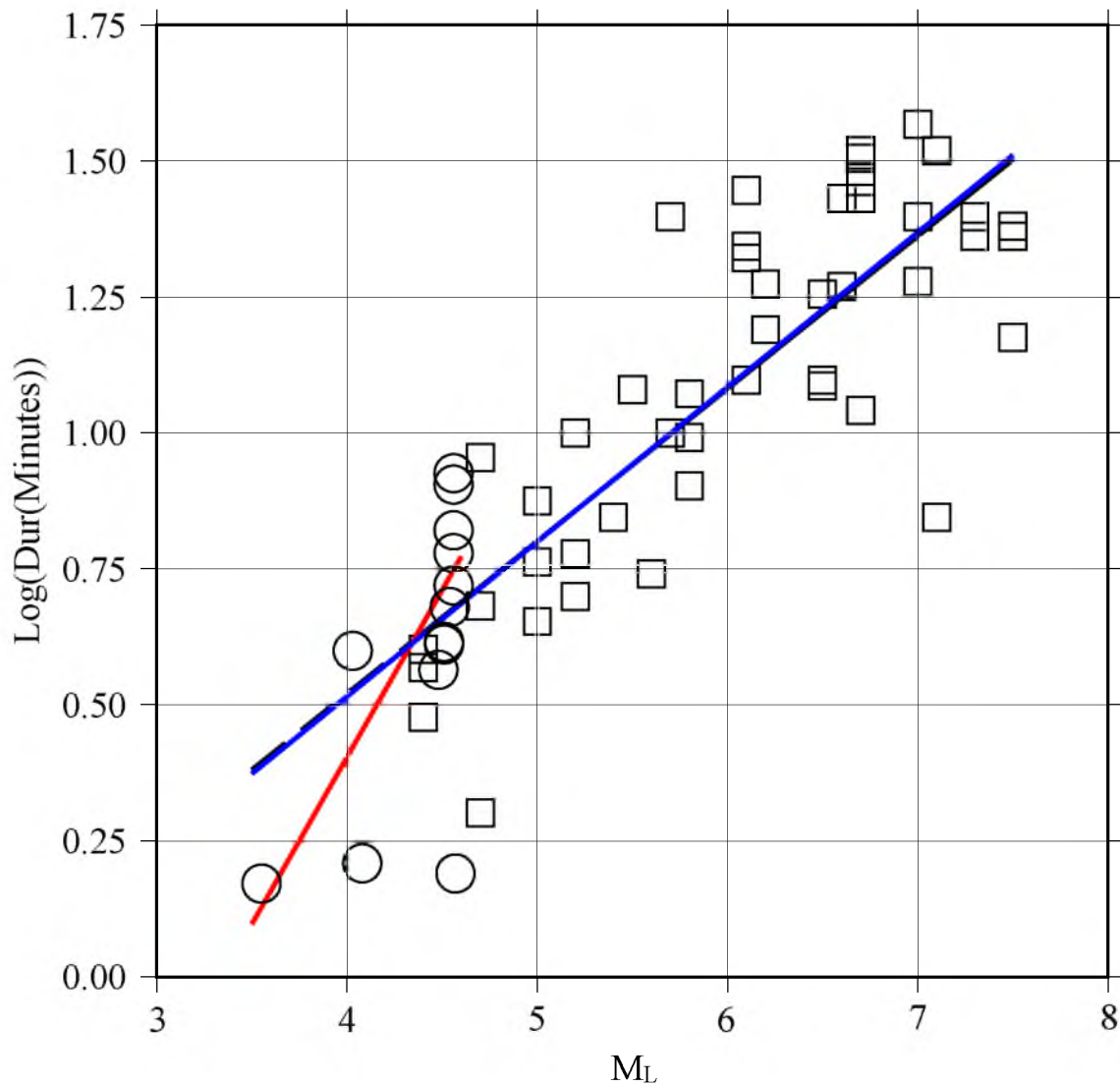
Figure 6.6. Log of the signal durations versus seismic magnitude. MW05 detections (squares) and the corresponding regression line (black, dashed black is the projection to *M*3.5). Detections identified in this study (circles) have a dramatically different relation (red). When the datasets are combined, the regression line for the combined datasets closely matches (blue) the original study.

$$\log(Duration) = 0.28M_L - 0.60 \tag{6.2}$$

They attribute the increase in duration with magnitude to an increased area exceeding the PGA threshold.

We measured durations from earthquakes with magnitudes $3.55 \leq M \leq 4.57$. The fit to this data set suggests a separate relation for smaller magnitude events of

$$\log(Duration) = 0.61M_L - 2.1 \tag{4}$$

However, when the data sets are combined, the least squares fit (blue) is nearly identical to the original relation from MW05 (black line),

$$\log(Duration) = 0.28M_L - .62 \tag{6}$$

When performing the standard deviation test, as was done for the amplitude versus magnitude relations, there is no statistically significant difference.

6.5. Other Data Trends

In an effort to link different variables, multiple comparisons were attempted though the complex interaction of all variables made identifying unique correlations difficult. There is a need for more data to identify trends across distance, magnitude, path, depth, frequency, amplitude, duration, detection, and nondetection. To explore the possibility of infrasound as a depth discriminant, we correlated depth and peak frequency similarly to MW05 (Figure 6.7a). There is significant scatter for frequencies from 1 to 5.7 Hz for our data (circles) and we are unable to draw any definitive correlation between frequency and depth. When combined with MW05 data (squares), there appears to be a
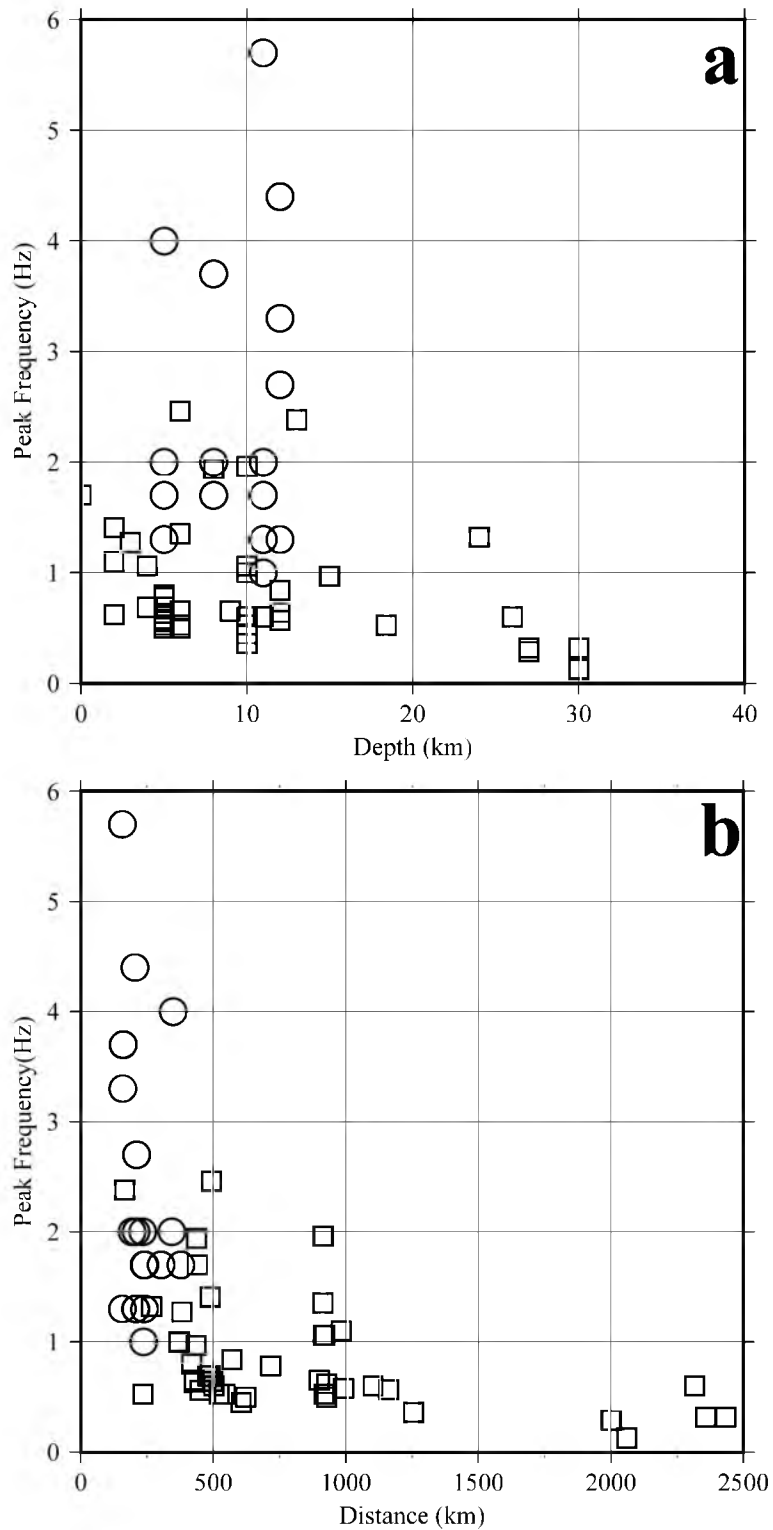
Figure 6.7. Frequency versus (a) depth and (b) distance. MW05 data (squares) extend to greater depth and distances. When combined with detections from this study (circles), we see a possible relation with depth, though we must keep in mind the dispersion of higher frequencies with distance.

trend toward lower frequencies with increased depth down to 30 km. A more obvious

decay exists for frequency as a function of increasing distance. However, it is important

to note that frequency is expected to decrease with distance due to absorption in the

atmosphere (Figure 6.7b).

CHAPTER 7

DISCUSSION

7.1 Optimal Location Versus Thresholds for Observations

In Figure 6.4, we show a discrepancy between the number of events meeting the

threshold for generating infrasound and corresponding detections. Given these data, it

may be concluded that our arrays are not optimally located to detect epicentral

infrasound. For example, the M_W4.5 Randolph, UT earthquake (#210 Table 3.1,

Appendix B) was widely felt throughout northern Utah and parts of Wyoming and Idaho.

The event mechanism is normal faulting on a generally north-striking fault. The event

had significant ground motions with observed PGA of 7 cm s^{-2} at the nearest station

(HWU, Δ = 38 km) and an estimated PGA of 115 cm s^{-2} at the epicenter (Hale *et al.*,

2010). Using Chiou *et al.* (2010), the maximum epicentral distance exceeding the

conservative MW05 threshold (20 cm s^{-2}) is 21 km, an area of approximately 1,400 km^2.

However, no infrasound arrivals were detected for the Randolph earthquake at any of the

three operating arrays (BGU, EPU, and NOQ) at distances ranging from 115 km to 185

km. G2S profiles were extracted for the time of the earthquake in the direction of the

three installed arrays (Figure 7.1, blue lines) as well as BRP (red line). The thermosphere

(~110 km) is the only layer to exceed the soundspeed at the surface (~350 m s^{-1}), which

would result in returns beyond 250 km, greater than the distance to all three arrays. The

atmospheric profile for BRP is closer to the required surface soundspeed for a
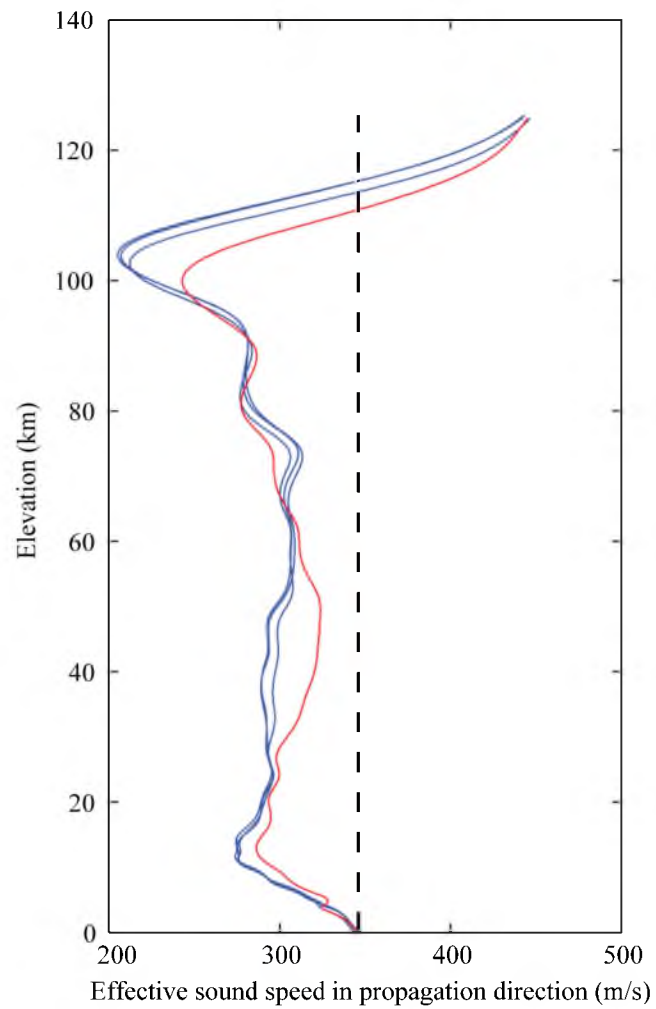
Figure 7.1. G2S profiles for earthquake # 210 in the directions of the three operational infrasound arrays (BGU, EPU, and NOQ; blue) and BRP (red), which was scheduled for installation the following day. Ground soundspeed shown in vertical bold dashed line.

stratospheric return. A detection at BRP may have been possible with localized ducting and accounting for the geophysical uncertainties at the stratopause (Arrowsmith *et al.*, 2010). Unfortunately, BRP was scheduled to be deployed the following day. The three arrays have similar paths and are along the same general azimuth (south – southwest). This example highlights the need for a dense network of arrays with varying azimuthal and distance coverage to maximize the likelihood of detection.

Requiring more than one detection provides an additional constraint on whether the infrasound originated at the epicenter by providing crossing backazimuths near the source. Allowing single detections would introduce additional error and scatter into the relations. Of the 43 medium and large earthquakes contributing to the MW05 scaling relationships between 1983 and 2005, only 16 have multiple detections due to sparse infrasound array spacing. It is possible that single array observations are erroneously attributed to earthquakes in previous studies. In future studies, it will be important to evaluate the scatter from multiple infrasound detections in order to assess the applicability of using single event detections. This highlights the need for increasing both the data collection time period and the sampling density of infrasound arrays.

7.2 Duration Relation Slope Change

In Figure 6.7, there appears to be a slope change around $4.0 \leq M \leq 5.0$, perhaps caused by a lack of sampling at lower magnitudes. Given the PGA requirement of $10 - 20$ cm s^{-2} from MW05, we explore a physical explanation at the epicentral region. We calculate predicted PGA values for fixed depth and Vs30 over a range of distances and magnitudes to see the extent that the MW05 threshold is exceeded for earthquakes near the surface. Figure 7.2 shows PGA contours in 10 cm s^{-2} increments plotted with distance
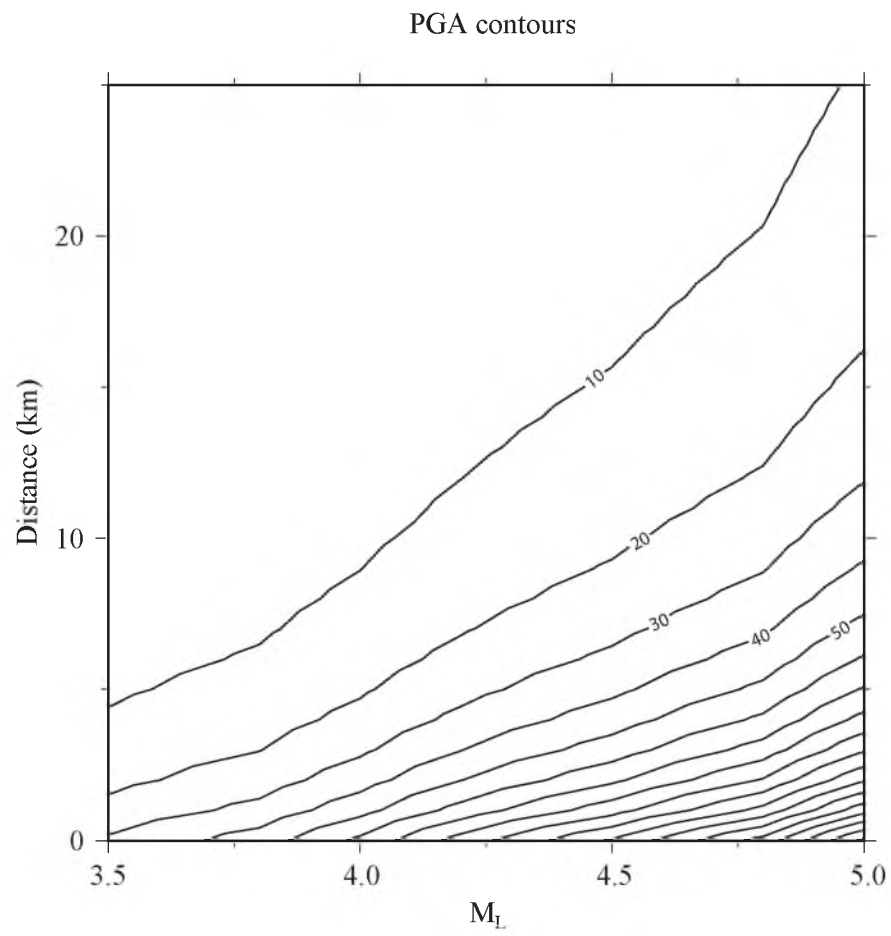
PGA contours

Figure 7.2. Predicted PGA contours (cm s^{-2}) plotted as a function of distance and magnitude.

(km) and magnitude. At $M_L3.6$ and $M_L4.6$, there are abrupt changes in the pattern of PGA and distance. PGA increases with distance more rapidly after each of these magnitudes. MW05 proposed that duration is proportional to the epicentral area exceeding the 10 -20 cm s^{-2} threshold. This is contrary to what we see in Figure 7.2. The change in slope for duration versus magnitude for small events (Figure 6.6) could be due to atmospheric paths, source characteristics, or differences in methods used for duration measurements between this study and MW05.

CHAPTER 8

CONCLUSIONS

Deploying a dense network of infrasound arrays in an active seismogenic zone,
we collected close to three years of data with three permanent arrays, and two years with
nine temporary arrays. Each earthquake (total number = 293) was processed
systematically using the batch processing feature in InfraMonitor to look specifically for
infrasound signals occurring in the epicentral time window (group velocities of 0.22 –
0.35 m s^{-1}). Of these, nine earthquakes $3.55 \leq M \leq 5.91$ with depths of 5 -12 km had
detections at multiple arrays at distances between 156 – 695 km. These contributions can
be added to the points and relations of MW05 and Le Pichon *et al.* (2006). We also
update the techniques used to measure, correct, and characterize epicentral infrasound
signals in a detailed reproducible manner.

With the addition of our measurements, we propose extending the MW05
relations to lower magnitudes. Further data collection with increased sampling is
necessary to resolve the difference in slope of duration versus magnitude for smaller
magnitude events. We see a slight difference in the earthquake detections between winter
and summer.

Like MW05, this study attempted to correlate various variables. We explore a
possible relation between the frequency of the detected infrasound signal and earthquake
depth. However, we attribute the frequencies to be more strongly correlated to the

distance of the observation to the earthquake. The absorption of frequency with distance is known and additional data from earthquakes of the same magnitude with varying depths is needed to develop a relation between depth and frequency.

With the sampling coverage and distribution of earthquakes in this study, the small number of detected earthquakes suggests that infrasound observations are not a robust method of detecting small earthquakes or characterizing earthquake sources. However, this study suggests strong potential for the use of infrasound as a discriminant, particularly for low magnitude seismic events.

Though sampling limitations are certainly a factor, we see no clear relation between infrasound generation and faulting style. The infrasound generation from a strike-slip event could be caused by the MW05 PGA threshold being exceeded in the epicentral region and the lateral motion effecting topographic features rather than a vertical pumping of the atmosphere.

Future research should include greater azimuthal array coverage to account for seasonal variations in atmospheric paths, arrays extending to greater distances, co-locating infrasound sensors with preexisting seismic sensors and increasing data collection time.

APPENDIX A

Locations and elevations for each infrasound gauge in the Utah network of infrasound arrays.

Table A.1 Array element locations

Channel	Latitude	Longitude	Elevation (km)
BGU1	40.9204	-113.0309	1.640
BGU2	40.9207	-113.0301	1.640
BGU3	40.9203	-113.0293	1.640
BGU4	40.9215	-113.0299	1.640
BRP1	39.4727	-110.7409	1.673
BRP2	39.4738	-110.7405	1.683
BRP3	39.4729	-110.7391	1.681
BRP4	39.4730	-110.7400	1.681
EPU1	41.3901	-112.4099	1.436
EPU2	41.3915	-112.4102	1.436
EPU3	41.3912	-112.4088	1.436
EPU4	41.3908	-112.4097	1.436
FSU1	39.7196	-113.3900	1.454
FSU2	39.7210	-113.3899	1.395
FSU3	39.7203	-113.3885	1.372
FSU4	39.7203	-113.3895	1.429
HWU1	41.6071	-111.5642	1.720
HWU2	41.6065	-111.5659	1.733
HWU3	41.6078	-111.5656	1.729
HWU4	41.6072	-111.5652	1.728
LCM1	37.0109	-113.2444	1.407
LCM2	37.0105	-113.2428	1.405
LCM3	37.0118	-113.2430	1.407
LCM4	37.0111	-113.2434	1.402
NOQ3	40.6526	-112.1186	1.591
NOQ4	40.6527	-112.1205	1.629
NOQ5	40.6537	-112.1193	1.614
NOQ6	40.6530	-112.1195	1.621

Table A.1 (continued)

Channel	Latitude	Longitude	Elevation (km)
PSU1	38.5332	-113.8555	2.005
PSU2	38.5344	-113.8551	2.003
PSU3	38.5334	-113.8538	1.981
PSU4	38.5337	-113.8547	1.997
WMU1	40.0795	-111.8310	2.001
WMU2	40.0798	-111.8294	2.024
WMU3	40.0785	-111.8299	2.006
WMU4	40.0792	-111.8300	2.015

APPENDIX B

Catalog of earthquakes used in this study are numbered in chronological order. Numbering is consistent with earthquakes in the text and tables of this paper. UUSS moment tensors solutions (Whidden and Pankow, 2012) are calculated using a full moment tensor inversion (Minson and Dreger, 2008). Focal mechanism parameters shown for moment tensors where UUSS solutions are unavailable are taken from the Saint Louis University Earthquake Center catalog of double-couple moment tensors (Hermann *et al.*, 2011; *italicized*). Vs30 values for earthquakes occurring in Utah are taken from McDonald and Ashland (2008). For earthquakes outside of the Utah region, we use values available from the Global Vs30 Map Server for active tectonic regions (Allen and Wald, 2009; *italicized*). Predicted ground motions for earthquakes from $3.0 \leq M < 5.0$ are calculated according to Chiou *et al.*, (2010). For earthquakes $M \geq 5.0$, we calculate predicted ground motions using relations in Chiou and Youngs (2008; *italicized*).

Table B.1. Earthquake catalog

#	Origin Time	Latitude (°)	Longitude (°)	Depth (km)	M_L
1	2007 04 27 15:42:49	37.0795	-115.2650	0.71	3.9
2	2007 05 08 15:46:48	45.4297	-112.1320	0.26	4.66
3	2007 05 19 17:18:48	38.8650	-107.5170	1.74	3.54
4	2007 06 02 05:11:25	33.8698	-116.1060	5.86	*4.33*
5	2007 06 05 03:28:42	41.6927	-109.9730	1.15	3.1
6	2007 06 05 03:29:06	41.5882	-109.9080	5.29	3.42
7	2007 06 11 01:03:46	37.4943	-114.0160	1.53	3.93
8	2007 06 11 08:13:48	42.6042	-111.3490	1.39	3.08
9	2007 06 14 02:40:42	45.4260	-112.6090	1.04	3.41
10	2007 07 04 04:03:24	37.5465	-112.5300	2.43	3.13
11	2007 07 04 18:31:58	37.5385	-112.5290	1.14	3.1
12	2007 07 05 11:44:08	43.3913	-109.3780	0.16	3.02
13	2007 07 16 23:09:34	45.3545	-112.6200	1.89	3.08
14	2007 08 06 05:59:44	37.7957	-114.3410	2.09	4.36

M_w	Depth (km)	Strike1/2 (°)	Dip1/2 (°)	Rake1/2 (°)	Vs30 (m s^{-1})	PGA (cm s^{-2})	PGV (cm s^{-1})
		Moment Tensor Results				Ground Motions CY 2010	
3.82	10	168/260	80/80	170/10	535	14.35	0.47
4.36	10	345/156	55/35	-85/-97	503	33.31	1.41
					706	25.10	0.96
					760	39.39	1.68
					1010	12.20	0.35
					1010	9.56	0.25
3.76	8	166/257	89/74	164/2	1010	11.87	0.33
					512	14.96	0.53
					410	30.33	1.40
					1010	9.62	0.26
					1010	12.23	0.35
					504	18.80	0.72
					338	15.87	0.63
					403	88.98	6.02

Table B.1, continued

#	Origin Time	Latitude (°)	Longitude (°)	Depth (km)	M_L
15	2007 08 06 08:48:40	39.4635	-111.2280	0.41	3.92
16	2007 08 18 13:14:25	36.4682	-110.3280	7.68	3.11
17	2007 08 18 13:16:30	38.0697	-113.3230	0.64	3.93
18	2007 08 21 16:17:54	36.5335	-110.3940	7.6	3.2
19	2007 09 01 18:32:02	41.6435	-112.3140	5.77	3.92
20	2007 10 28 13:35:26	43.4652	-110.4990	0.67	3.26
21	2007 10 31 05:23:22	43.2888	-110.1850	4.35	3.87
22	2007 11 03 15:45:43	38.9565	-107.6700	1.7	3.08
23	2007 11 05 21:48:00	39.3458	-111.6470	5.5	3.91
24	2007 11 22 02:29:36	41.6330	-109.7360	4.72	3.42
25	2007 12 02 01:38:36	38.9173	-107.5750	1.14	3.52
26	2007 12 05 00:22:41	36.4422	-113.1360	6.2	3.46
27	2007 12 10 05:46:13	37.5308	-112.3220	1.9	3
28	2007 12 12 18:07:24	37.3607	-114.1130	1.12	3.06

		Moment Tensor Results				Ground Motions CY 2010	
M_w	Depth (km)	Strike1/2 (°)	Dip1/2 (°)	Rake1/2 (°)	Vs30 (m s^{-1})	PGA (cm s^{-2})	PGV (cm s^{-1})
4.16	1	11/217	60/33	-104/-67	1460	56.91	2.60
					453	6.05	0.17
3.71	6	64/208	75/18	-79/-125	234	25.23	1.26
					309	8.36	0.27
3.83	10	244/154	90/89	1/180	234	20.42	0.91
					760	20.35	0.72
					534	28.87	1.23
					722	12.00	0.37
3.82	11	23/220	68/22	-96/-75	234	18.65	0.80
					1010	10.38	0.28
					707	27.93	1.10
					388	13.67	0.50
					1010	8.63	0.23
					1010	11.49	0.33

Table B.1, continued

#	Origin Time	Latitude (°)	Longitude (°)	Depth (km)	M_L
29	2007 12 13 07:54:45	37.3615	-114.1110	0.52	3.46
30	2007 12 27 00:13:20	36.5322	-112.2390	7.14	3.07
31	2007 12 31 03:29:21	44.7872	-110.9460	4.9	3.62
32	2008 01 09 21:37:37	44.7813	-110.9420	4.4	3.73
33	2008 01 18 23:06:30	36.4985	-114.5160	3.66	3.05
34	2008 02 01 06:52:28	38.1963	-112.2070	0.18	3.59
35	2008 02 01 21:36:54	41.8087	-112.2180	6.23	3.54
36	2008 02 09 17:41:49	41.6677	-109.8890	1.73	3.32
37	2008 02 21 14:16:02	41.1332	-114.8620	7.6	5.91
38	2008 02 21 14:34:41	41.1495	-114.8680	5.7	4.51
39	2008 02 21 14:46:31	41.1440	-114.8800	3.62	3.37
40	2008 02 21 14:59:07	41.1002	-114.8690	10	3.13
41	2008 02 21 15:06:09	41.1442	-114.8180	0.29	3.22
42	2008 02 21 15:10:33	41.1397	-114.9150	5.08	3.12

		Moment Tensor Results				Ground Motions CY 2010	
M_w	Depth (km)	Strike1/2 (°)	Dip1/2 (°)	Rake1/2 (°)	Vs30 (m s^{-1})	PGA (cm s^{-2})	PGV (cm s^{-1})
					1010	25.57	0.91
					418	6.21	0.18
					531	18.33	0.68
					503	23.86	0.97
					392	10.06	0.34
					234	59.32	4.04
					2197	9.74	0.25
					1010	15.27	0.47
5.88	11	205/25	50/40	-90/-90	370	246.37	18.86
4.29	11	40/177	60/38	-65/-126	368	31.68	1.41
					348	18.02	0.74
					441	5.06	0.13
					663	22.47	0.85
					353	9.47	0.32

#	Origin Time	Latitude (°)	Longitude (°)	Depth (km)	M_L
43	2008 02 21 15:11:47	41.1445	-114.9020	6.89	3.51
44	2008 02 21 15:34:25	41.1355	-114.8700	6.75	3.94
45	2008 02 21 15:43:14	41.1368	-114.8790	7.91	3.04
46	2008 02 21 15:48:22	41.1320	-114.9120	6.54	3.09
47	2008 02 21 15:50:27	41.1525	-114.8610	8.2	3.35
48	2008 02 21 16:05:53	41.1915	-114.9210	1.87	3.37
49	2008 02 21 16:14:16	41.2078	-114.8420	6.23	3.54
50	2008 02 21 16:20:01	41.1163	-114.7070	11.06	4.1
51	2008 02 21 16:23:17	41.1757	-114.9180	1.5	3.33
52	2008 02 21 16:25:49	41.0992	-114.9090	7.91	3.63
53	2008 02 21 16:39:28	41.1245	-114.9190	4.81	3.69
54	2008 02 21 17:16:13	41.1635	-114.8260	8.19	3.24
55	2008 02 21 17:21:30	41.1190	-114.8520	9.65	3.11
56	2008 02 21 18:55:52	41.1580	-114.8270	7.85	3.02

	Moment Tensor Results					Ground Motions CY 2010	
M_w	Depth (km)	Strike1/2 (°)	Dip1/2 (°)	Rake1/2 (°)	Vs30 (m s^{-1})	PGA (cm s^{-2})	PGV (cm s^{-1})
					320	14.76	0.57
3.69	10	187/20	51/40	-98/80	350	13.98	0.50
					351	5.85	0.17
					341	7.53	0.24
					410	8.92	0.28
					760	18.16	0.62
					544	13.41	0.45
3.89	11	225/354	55/48	-55/-129	404	16.68	0.60
					713	19.05	0.67
					415	14.35	0.51
					330	25.08	1.15
					646	6.11	0.15
					421	5.15	0.13
					572	4.60	0.11

#	Origin Time	Latitude (°)	Longitude (°)	Depth (km)	M_L
57	2008 02 21 19:37:08	41.1297	-114.9210	5.26	3.47
58	2008 02 21 19:53:48	41.1445	-114.9360	3.03	3.59
59	2008 02 21 19:57:19	41.1168	-114.9230	3.91	3.61
60	2008 02 21 20:04:58	41.1805	-114.8560	7.44	3.47
61	2008 02 21 20:37:38	41.2148	-114.8630	6.85	3.26
62	2008 02 21 21:35:50	41.1318	-114.9440	6.2	3.23
63	2008 02 21 22:17:19	41.1547	-114.8770	6.7	3.21
64	2008 02 21 23:02:52	41.1202	-114.8180	10.97	3.16
65	2008 02 21 23:57:50	41.1450	-114.9230	4.42	4.78
66	2008 02 21 00:02:51	41.1740	-114.9230	1.76	3.19
67	2008 02 22 00:14:59	41.1267	-114.9310	3.32	3.31
68	2008 02 22 01:50:05	41.1282	-114.8740	8.08	4.03
69	2008 02 22 05:07:22	41.1737	-114.9360	2.81	3.56
70	2008 02 22 07:33:35	41.1488	-114.9140	3.8	3.45

M_w	Moment Tensor Results				Vs30 $(m\ s^{-1})$	Ground Motions CY 2010	
	Depth (km)	Strike1/2 (°)	Dip1/2 (°)	Rake1/2 (°)		PGA $(cm\ s^{-2})$	PGV $(cm\ s^{-1})$
					341	16.57	0.66
					404	26.44	1.17
					330	25.44	1.17
					476	11.03	0.35
					347	9.57	0.32
					285	10.70	0.39
					352	8.91	0.29
					375	5.28	0.14
4.61	*9*	*19/255*	*68/35*	*-118/-40*	*344*	58.86	3.31
					569	15.77	0.55
					329	17.64	0.73
3.86	*11*	*230/5*	*55/45*	*-60/-126*	*361*	16.67	0.62
					685	21.11	0.77
					287	21.41	0.97

Table B.1, continued

#	Origin Time	Latitude (°)	Longitude (°)	Depth (km)	M_L
71	2008 02 22 09:17:05	41.1687	-114.9720	5.68	3
72	2008 02 22 10:27:10	41.1623	-114.9290	3.62	3.37
73	2008 02 22 10:30:40	41.1712	-114.9490	3.04	3.09
74	2008 02 22 11:05:29	41.1955	-114.9210	2.35	3.51
75	2008 02 22 11:09:30	41.1808	-114.9510	3.17	3.26
76	2008 02 22 11:17:24	41.1772	-114.9390	3.09	3.53
77	2008 02 22 15:30:23	41.1347	-114.8530	7.68	3.54
78	2008 02 22 17:10:20	41.1283	-114.8660	7.53	3.42
79	2008 02 22 17:31:44	41.1245	-114.8950	8.25	3.38
80	2008 02 22 18:30:19	41.1268	-114.8810	7.83	3.35
81	2008 02 22 19:22:29	41.1188	-114.8990	5.97	3.69
82	2008 02 22 21:33:03	41.1875	-114.8860	4.86	3.01
83	2008 02 22 23:24:03	41.1078	-114.9150	7.88	3.55
84	2008 02 22 23:27:45	41.1055	-114.9000	7.35	4.48

| | Moment Tensor Results | | | | | Ground Motions CY 2010 | |
M_w	Depth (km)	Strike1/2 (°)	Dip1/2 (°)	Rake1/2 (°)	Vs30 (m s^{-1})	PGA (cm s^{-2})	PGV (cm s^{-1})
					569	5.78	0.15
					515	15.31	0.54
					680	9.50	0.28
					742	20.65	0.74
					615	12.86	0.42
					760	18.30	0.63
					393	13.04	0.46
					370	11.21	0.38
					366	9.79	0.32
					349	9.93	0.33
					366	20.64	0.86
					340	8.24	0.27
					374	13.24	0.47
4.32	12	38/225	50/40	-94/-85	415	29.64	1.23

Table B.1, continued

#	Origin Time	Latitude (°)	Longitude (°)	Depth (km)	M_L
85	2008 02 23 08:38:56	41.1723	-114.9140	2.77	3.07
86	2008 02 23 22:56:38	41.2867	-114.8670	5.01	3.44
87	2008 02 24 18:15:58	41.1453	-114.9020	3.65	3.02
88	2008 02 25 05:51:55	41.0743	-114.9210	12.03	3.02
89	2008 02 25 20:49:21	41.1490	-114.8950	9.64	3.11
90	2008 02 26 02:22:23	41.2455	-114.8710	5.93	3.58
91	2008 02 26 02:48:45	41.2817	-114.8680	8.21	3.39
92	2008 02 26 03:47:14	41.2920	-114.8640	4.71	3.38
93	2008 02 26 11:53:14	41.1943	-114.8880	4.8	3.44
94	2008 02 27 07:59:37	41.2033	-114.8510	6.35	4.47
95	2008 02 27 20:06:33	41.0807	-114.8950	7.93	3.21
96	2008 02 28 12:36:45	41.1853	-114.9020	6.18	3.06
97	2008 02 28 15:10:37	41.1392	-114.9180	2.13	4.04
98	2008 02 29 07:19:11	41.2008	-114.8600	5.55	3.27

| | Moment Tensor Results | | | | | Ground Motions CY 2010 | |
M_w	Depth (km)	Strike1/2 (°)	Dip1/2 (°)	Rake1/2 (°)	Vs30 (m s^{-1})	PGA (cm s^{-2})	PGV (cm s^{-1})
					494	11.10	0.36
					371	15.80	0.61
					320	10.43	0.37
					485	3.44	0.08
					356	5.54	0.15
					470	15.78	0.57
					396	9.66	0.31
					364	15.12	0.58
					389	15.98	0.61
4.12	*11*	*90/359*	*85/80*	*10/175*	*477*	22.15	0.83
					640	6.00	0.15
					516	6.26	0.17
3.98	*10*	*22/250*	*61/40*	*-118/-50*	*312*	22.90	0.98
					431	10.46	0.34

Table B.1, continued

#	Origin Time	Latitude (°)	Longitude (°)	Depth (km)	M_L
99	2008 02 29 08:49:47	41.1092	-114.9130	7	3.57
100	2008 03 01 13:57:03	41.1902	-114.8610	5.42	3.34
101	2008 03 03 22:40:04	41.1877	-114.8640	5.54	3.23
102	2008 03 03 22:45:03	41.1900	-114.8650	4.94	3.6
103	2008 03 06 02:05:55	41.1928	-114.8750	4.63	3.16
104	2008 03 14 07:39:05	41.1290	-114.9130	7.25	3.21
105	2008 03 15 16:22:33	41.1273	-114.9050	10.09	3.62
106	2008 03 19 09:32:30	36.5202	-113.5100	0.56	3.26
107	2008 03 25 09:22:04	45.2965	-112.5140	1.36	3.14
108	2008 03 25 11:59:37	44.6915	-110.0150	0.06	4.2
109	2008 03 27 01:07:13	36.5012	-113.5340	7.32	4.01
110	2008 04 01 13:16:17	41.2257	-114.8440	9.02	4.54
111	2008 04 15 13:37:59	37.1950	-115.0920	1.11	3.41
112	2008 04 22 19:33:17	36.6470	-108.4410	3.21	3.19

| | Moment Tensor Results | | | | | Ground Motions CY 2010 | |
M_w	Depth (km)	Strike1/2 (°)	Dip1/2 (°)	Rake1/2 (°)	Vs30 (m s^{-1})	PGA (cm s^{-2})	PGV (cm s^{-1})
					360	15.27	0.58
					433	11.91	0.41
					433	9.78	0.32
					433	19.24	0.76
					442	9.84	0.32
					341	8.47	0.27
3.57	10	232/45	45/45	-85/-95	340	11.70	0.40
					379	28.01	1.29
					340	19.72	0.84
4.21	12	111/5	64/60	-146/-30	760	19.48	0.62
3.72	10	220/332	70/44	-50/-150	348	14.69	0.54
4.12	12	185/85	79/50	-139/-15	347	23.56	0.96
					397	30.20	1.40
					376	14.02	0.52

Table B.1, continued

#	Origin Time	Latitude (°)	Longitude (°)	Depth (km)	M_L
113	2008 04 22 20:40:08	41.2237	-114.8450	4.94	4.32
114	2008 04 23 08:53:58	38.5537	-107.8300	8.37	3.02
115	2008 05 14 06:42:11	42.8300	-111.2400	7.7	3.02
116	2008 05 21 23:57:07	37.5343	-112.3170	1.18	3.04
117	2008 06 04 23:32:35	36.4560	-112.5090	2.77	3.84
118	2008 06 06 20:09:59	37.3578	-109.4680	9.59	3.66
119	2008 06 15 19:27:22	41.7377	-112.6100	7.02	3.09
120	2008 06 30 22:49:58	37.3655	-114.3190	0.99	3.7
121	2008 07 22 09:32:51	42.9015	-111.2580	6.01	3.4
122	2008 08 12 10:58:45	41.1742	-114.8420	7.03	3
123	2008 08 16 02:24:23	42.4788	-111.5870	4.54	3.26
124	2008 08 20 16:06:59	46.1998	-111.2900	2.64	3.43
125	2008 08 20 19:43:13	46.1455	-111.2960	1.52	3.59
126	2008 08 28 19:26:27	37.5353	-112.3170	0.12	3.29

| | Moment Tensor Results | | | | | Ground Motions CY 2010 | |
Mw	Depth (km)	Strike1/2 (°)	Dip1/2 (°)	Rake1/2 (°)	Vs30 (m s⁻¹)	PGA (cm s⁻²)	PGV (cm s⁻¹)
3.83	*11*	*186/45*	*66/30*	*-108/-55*	*445*	14.59	0.49
					383	5.19	0.14
					756	4.13	0.09
					1010	10.94	0.31
					760	30.82	1.24
3.29	13	123/323	75/15	-95/-71	1460	3.52	0.06
					234	8.34	0.29
					529	42.53	2.06
3.34	*6*	*314/50*	*76/65*	*154/15*	*485*	10.51	0.34
					592	4.79	0.12
					2197	7.82	0.19
					577	19.18	0.71
					472	33.60	1.55
					1010	21.98	0.75

#	Origin Time	Latitude (°)	Longitude (°)	Depth (km)	M_L
127	2008 08 30 22:06:15	41.6737	-111.1450	2.81	3.31
128	2008 08 31 13:57:38	42.9082	-111.2570	0.3	3.16
129	2008 09 07 02:12:12	41.7118	-112.3790	2.42	3.08
130	2008 10 02 22:55:09	37.3542	-114.5480	1.7	3.31
131	2008 10 12 03:26:01	41.6903	-111.1420	8.59	3.37
132	2008 10 19 19:51:17	35.6242	-111.7150	6.36	3.43
133	2008 12 27 20:17:33	44.4885	-110.3560	1.78	3.41
134	2008 12 27 20:26:27	44.5077	-110.3640	1.08	3.15
135	2008 12 27 22:30:03	44.5005	-110.3620	0.93	3.33
136	2008 12 28 05:15:56	44.5045	-110.3640	0.24	3.87
137	2008 12 28 09:23:57	44.5117	-110.3590	0.03	3.23
138	2008 12 28 19:32:15	44.5110	-110.3580	0.01	3.01
139	2008 12 28 19:55:17	44.5112	-110.3520	0.12	3.04
140	2008 12 29 19:14:48	44.5225	-110.3700	0.19	3.25

| | | Moment Tensor Results | | | | Ground Motions CY 2010 | |
M_w	Depth (km)	Strike1/2 (°)	Dip1/2 (°)	Rake1/2 (°)	Vs30 (m s^{-1})	PGA (cm s^{-2})	PGV (cm s^{-1})
3.29	10	10/245	60/45	-125/-45	234	8.68	0.30
					485	23.19	0.95
					234	16.48	0.73
					466	21.12	0.84
					234	11.22	0.43
					281	14.59	0.58
					150	37.02	2.39
					150	29.24	1.74
					150	39.66	2.63
					150	91.59	8.69
					150	42.96	2.95
					150	30.85	1.89
					150	31.39	1.93
					150	42.39	2.89

Table B.1, continued

#	Origin Time	Latitude (°)	Longitude (°)	Depth (km)	M_L
141	2008 12 31 09:02:28	44.5248	-110.3610	1.9	3.58
142	2008 12 31 15:02:11	44.5222	-110.3630	1.63	3.2
143	2009 01 02 01:13:05	44.5607	-110.3680	0.75	3.08
144	2009 01 02 01:21:19	44.5592	-110.3670	1.69	3.1
145	2009 01 02 18:32:49	44.5508	-110.3610	1.14	3.43
146	2009 01 02 19:40:54	44.5482	-110.3750	0.42	3.05
147	2009 01 02 20:15:39	44.5270	-110.3670	0.66	3.08
148	2009 01 04 15:29:28	41.1983	-114.7680	7.07	3.94
149	2009 01 09 18:17:31	44.6768	-110.2530	0.85	3.31
150	2009 01 16 04:15:34	43.2138	-111.0130	1.35	4.08
151	2009 01 19 13:40:09	37.3855	-114.6130	13.37	3.06
152	2009 01 31 13:43:37	42.3378	-111.1840	1.12	3.11
153	2009 02 11 20:18:00	36.8673	-108.6900	11.54	3.13
154	2009 02 14 23:17:03	45.5265	-111.8840	1.44	3.26

| | Moment Tensor Results | | | | | Ground Motions CY 2010 | |
M_w	Depth (km)	Strike1/2 (°)	Dip1/2 (°)	Rake1/2 (°)	Vs30 (m s^{-1})	PGA (cm s^{-2})	PGV (cm s^{-1})
					150	45.84	3.22
					150	27.93	1.64
					313	21.47	0.96
					313	17.69	0.74
					307	34.07	1.76
					150	29.42	1.77
					150	29.01	1.73
					371	26.35	1.17
					290	31.11	1.58
4.02	*8*	*4/190*	*55/35*	*-93/-85*	760	20.03	0.68
					523	3.27	0.07
					1460	11.90	0.33
					363	4.88	0.13
					535	19.52	0.74

#	Origin Time	Latitude (°)	Longitude (°)	Depth (km)	M_L
155	2009 03 06 11:29:54	45.6927	-112.1250	2.08	4.31
156	2009 03 06 11:33:05	45.6777	-112.1070	1.12	3.19
157	2009 03 07 02:45:10	41.6702	-109.9230	4.51	3.51
158	2009 03 09 03:20:23	38.8182	-111.7350	2.81	3.03
159	2009 03 14 03:58:38	45.6977	-112.1140	1.51	3.45
160	2009 03 21 08:47:49	43.3043	-110.7890	0.96	3.27
161	2009 03 23 05:43:26	37.4200	-113.1650	3.54	*3.21*
162	2009 03 31 02:36:10	37.6620	-110.4540	7.21	3
163	2009 04 08 21:15:11	36.5442	-110.3080	6.64	3.28
164	2009 05 17 06:45:19	42.5620	-108.2540	6.82	4.35
165	2009 06 03 21:47:01	41.8040	-112.2140	7.49	4.01
166	2009 06 30 15:52:06	44.7463	-110.7900	3.19	3.28
167	2009 07 02 00:15:18	37.0098	-114.4300	5.46	3.18
168	2009 07 13 03:40:37	37.0120	-110.7720	3.04	3.3

M_w	Depth (km)	Strike1/2 (°)	Dip1/2 (°)	Rake1/2 (°)	Vs30 (m s⁻¹)	Ground Motions CY 2010	
		Moment Tensor Results				PGA (cm s⁻²)	PGV (cm s⁻¹)
					644	70.66	3.90
					760	16.18	0.54
					1010	12.36	0.35
					234	14.05	0.59
					760	22.31	0.81
3.35	6	144/50	76/75	-164/-15	760	8.79	0.24
					1460	8.49	0.21
					1460	3.53	0.07
					396	9.59	0.31
3.7	17	71/310	73/30	-115/-35	278	10.35	0.32
					2197	17.44	0.53
					353	16.72	0.67
					631	7.73	0.21
					234	20.89	0.99

Table B.1, continued

#	Origin Time	Latitude (°)	Longitude (°)	Depth (km)	M_L
169	2009 07 20 05:31:50	37.4838	-114.5130	1.96	3.42
170	2009 08 08 02:14:18	44.8787	-111.7330	6.49	3.48
171	2009 09 04 11:47:53	36.6697	-112.8680	2.83	3.3
172	2009 10 17 15:48:19	44.4022	-114.1260	0.83	3.21
173	2009 10 17 20:21:38	44.4088	-114.1490	4.64	3.03
174	2009 11 09 11:02:04	39.8028	-114.7510	7.04	3.23
175	2009 11 09 17:49:15	44.7078	-110.2770	0.25	3.11
176	2009 11 13 13:22:37	38.9923	-111.3920	0.49	3.19
177	2009 12 04 03:54:43	44.7932	-112.3300	6.32	3.4
178	2010 01 01 04:13:29	42.6307	-111.0780	2.34	3.35
179	2010 01 04 16:24:03	37.5987	-113.0390	6.83	4.12
180	2010 01 05 04:55:24	37.5930	-113.0460	7.2	3.33
181	2010 01 18 18:03:14	44.5593	-110.9670	7.04	3.09
182	2010 01 19 03:39:39	44.5635	-110.9680	6.22	3.33

M_w	Depth (km)	Strike1/2 (°)	Dip1/2 (°)	Rake1/2 (°)	Vs30 (m s^{-1})	Ground Motions CY 2010 PGA (cm s^{-2})	PGV (cm s^{-1})
					421	24.72	1.06
					743	10.31	0.30
					358	18.35	0.75
					497	21.58	0.86
					383	8.38	0.27
					343	8.95	0.29
					601	19.79	0.74
					1460	16.03	0.49
					760	9.16	0.25
					598	17.67	0.63
3.91	12	178/268	89/83	173/1	1460	10.29	0.25
					1460	6.17	0.14
					359	6.94	0.21
					330	11.83	0.43

#	Origin Time	Latitude (°)	Longitude (°)	Depth (km)	M_L
183	2010 01 19 04:42:14	44.5665	-110.9680	6.55	3.02
184	2010 01 19 16:48:32	44.5657	-110.9640	4.1	3.27
185	2010 01 19 21:32:31	44.5630	-110.9690	6.23	3.59
186	2010 01 20 01:35:37	44.5600	-110.9670	7.2	3.22
187	2010 01 20 04:41:03	44.5682	-110.9630	6.77	3.39
188	2010 01 21 06:01:51	44.5633	-110.9740	5.07	3.74
189	2010 01 21 06:16:19	44.5658	-110.9670	6.51	3.85
190	2010 01 22 05:38:40	44.5505	-110.9700	6.34	3.3
191	2010 01 23 22:01:26	43.5077	-110.1620	1.61	3.53
192	2010 01 25 06:09:46	44.5648	-110.9610	7.17	3.19
193	2010 01 25 06:21:34	44.5632	-110.9590	9.02	3.04
194	2010 01 25 10:27:36	44.5623	-110.9580	7.66	3.04
195	2010 01 27 01:28:42	44.5640	-110.9630	7.49	3.11
196	2010 01 27 19:52:17	44.5715	-110.9620	7.03	3.03

M_w	Depth (km)	Strike1/2 (°)	Dip1/2 (°)	Rake1/2 (°)	Vs30 (m s^{-1})	PGA (cm s^{-2})	PGV (cm s^{-1})
					330	6.77	0.21
					359	13.99	0.53
					330	17.87	0.73
					359	8.48	0.27
					407	11.17	0.38
					330	26.07	1.21
4.26	16	350/89	85/30	-60/-170	359	23.41	0.87
					345	10.89	0.38
3.54	8	359/200	71/20	-97/-70	584	10.65	0.32
					359	8.09	0.26
					359	5.18	0.14
					419	5.56	0.15
					359	6.82	0.21
					407	5.94	0.17

| | Moment Tensor Results | | | | | Ground Motions CY 2010 | |

Table B.1, continued

#	Origin Time	Latitude (°)	Longitude (°)	Depth (km)	M_L
197	2010 01 28 08:46:15	44.5737	-110.9710	7.54	3.22
198	2010 02 03 02:31:46	44.5560	-110.9390	1.84	3.12
199	2010 02 12 22:37:09	37.0918	-112.8920	11.89	3.02
200	2010 04 04 03:15:52	44.5985	-110.9910	3.6	3.31
201	2010 04 05 14:48:01	44.6005	-110.9800	5.49	3.02
202	2010 04 09 20:58:29	37.5347	-112.3070	1.61	*3.04*
203	2010 04 14 17:16:13	45.3572	-112.6030	2.29	3.62
204	2010 04 14 18:58:45	38.0337	-111.1130	2.71	3.92
205	2010 04 14 22:39:52	38.0400	-111.1180	5.02	3.06
206	2010 04 15 10:48:36	38.0437	-111.1130	2.63	3.15
207	2010 04 15 23:59:38	41.7033	-111.0940	7.88	4.9
208	2010 04 28 17:40:02	38.0348	-111.1150	5.01	3.21
209	2010 04 30 18:34:21	44.8017	-111.5360	9.57	3.23
210	2010 04 30 18:34:57	44.7925	-111.5310	7.9	3.39

| M_w | Moment Tensor Results | | | | Ground Motions CY 2010 | | |
	Depth (km)	Strike1/2 (°)	Dip1/2 (°)	Rake1/2 (°)	Vs30 (m s^{-1})	PGA (cm s^{-2})	PGV (cm s^{-1})
					399	7.80	0.24
					393	16.12	0.62
					1460	2.40	0.04
					459	14.64	0.53
					641	5.83	0.15
					1010	9.87	0.27
					357	33.33	1.64
3.75	16	163/341	53/37	-88/-92	1460	6.39	0.13
					1460	5.20	0.11
					1460	9.10	0.23
4.59	3	338/205	74/22	-106/-45	234	114.99	10.24
					1460	6.71	0.16
					412	6.41	0.18
					375	10.20	0.34

#	Origin Time	Latitude (°)	Longitude (°)	Depth (km)	M_L
211	2010 05 02 15:00:00	38.0373	-111.1140	4.92	3.63
212	2010 05 27 06:16:55	41.6888	-111.0870	0.36	3.07
213	2010 06 11 11:06:14	41.6833	-111.0760	0.14	3
214	2010 06 18 09:25:55	42.7238	-111.1110	6.84	3.53
215	2010 06 20 23:59:14	42.7650	-111.1200	1.25	*3.42*
216	2010 06 28 05:31:28	42.5398	-111.3720	0.71	3.08
217	2010 07 08 16:31:17	37.1350	-113.4540	7.08	3.25
218	2010 08 05 00:04:16	43.5875	-110.4300	0.24	5.17
219	2010 08 05 14:59:27	43.5978	-110.4140	0.09	4.31
220	2010 08 05 17:45:19	43.5843	-110.4270	0.77	3.37
221	2010 08 06 15:34:16	43.6002	-110.4100	3.62	3.48
222	2010 08 07 11:19:03	43.5937	-110.4080	1.18	3.79
223	2010 08 09 06:12:19	43.6017	-110.4220	5.84	3.27
224	2010 08 17 02:49:54	43.6038	-110.4210	4.68	4.38

	Moment Tensor Results					Ground Motions CY 2010	
M_w	Depth (km)	Strike1/2 (°)	Dip1/2 (°)	Rake1/2 (°)	Vs30 (m s^{-1})	PGA (cm s^{-2})	PGV (cm s^{-1})
					1460	13.36	0.38
					2197	13.61	0.39
					2197	12.87	0.37
					546	12.25	0.39
					760	22.63	0.83
					574	16.90	0.61
					1460	5.48	0.12
					648	242.64	20.75
4.16	9	40/136	80/61	-30/-168	507	26.77	1.08
3.27	8	147/50	71/70	-159/-20	648	6.54	0.17
3.37	8	35/141	70/53	-40/-155	451	9.04	0.28
3.68	8	25/130	75/47	-45/-159	505	14.16	0.48
					547	9.08	0.27
4.13	8	55/147	85/70	-20/-175	547	27.15	1.09

Table B.1, continued

#	Origin Time	Latitude (°)	Longitude (°)	Depth (km)	M_L
225	2010 08 17 09:22:18	43.5888	-110.4080	0.08	3.38
226	2010 08 18 12:51:43	37.6447	-113.2260	2.98	3.03
227	2010 08 18 12:52:31	37.6378	-113.2220	6.41	3.8
228	2010 09 07 10:08:26	44.9513	-111.7390	3.3	3.39
229	2010 09 10 21:16:15	43.1305	-110.7290	3.8	3.28
230	2010 09 12 20:09:43	43.1140	-110.6970	0.39	4.22
231	2010 09 12 20:20:02	43.1143	-110.7240	1.81	3.51
232	2010 09 12 22:20:29	43.1095	-110.6930	1.18	4.01
233	2010 09 13 02:43:52	43.1103	-110.7140	0.17	3.85
234	2010 09 20 00:47:21	43.6018	-110.4240	5.22	3.41
235	2010 10 13 19:18:14	43.0762	-110.7950	0.1	3.51
236	2010 10 24 17:43:58	43.6013	-110.3990	0.76	4.64
237	2010 10 26 01:24:15	43.6067	-110.4060	2.87	3.92
238	2010 10 26 04:12:46	43.6008	-110.3960	0.53	3.34

| | Moment Tensor Results | | | | | Ground Motions CY 2010 | |
M_w	Depth (km)	Strike1/2 (°)	Dip1/2 (°)	Rake1/2 (°)	Vs30 (m s^{-1})	PGA (cm s^{-2})	PGV (cm s^{-1})
3.35	*7*	*124/215*	*85/80*	*170/5*	*604*	8.60	0.24
					1010	7.29	0.18
3.66	9	198/94	72/54	-142/23	1010	9.21	0.23
					760	14.13	0.45
					453	13.56	0.48
3.96	*11*	*0/148*	*55/40*	*-70/-116*	*760*	14.20	0.42
					337	31.93	1.58
					760	53.56	2.59
3.78	11	162/15	50/45	-113/-65	613	11.76	0.35
3.43	7	146/240	76/75	164/15	547	10.23	0.31
					760	35.04	1.46
4.39	*9*	*35/136*	*70/62*	*-30/-157*	*587*	35.30	1.48
3.8	*8*	*133/0*	*51/50*	*-124/-55*	*464*	17.69	0.65
					587	26.80	1.09

Table B.1, continued

#	Origin Time	Latitude (°)	Longitude (°)	Depth (km)	M_L
239	2010 11 06 20:39:05	37.0103	-112.8790	11.19	3.05
240	2010 12 15 21:59:57	43.0692	-110.8000	0.82	3.29
241	2010 12 22 00:53:56	43.1083	-110.7080	0.1	3.49
242	2010 12 26 15:53:54	44.7363	-111.7350	7.67	3.05
243	2011 01 03 12:06:36	38.2473	-112.3400	5.4	4.56
244	2011 01 03 20:23:45	38.2378	-112.3380	1.83	3.24
245	2011 01 06 03:18:09	38.2612	-112.3330	3.4	3.13
246	2011 01 06 22:31:04	38.2622	-112.3340	2.92	3.46
247	2011 01 07 22:51:07	38.2570	-112.3310	0.86	3.26
248	2011 01 12 08:46:29	38.2385	-112.3410	4.73	3.58
249	2011 01 12 22:04:53	42.1202	-111.5430	3.23	*3.1*
250	2011 01 20 21:59:12	39.1622	-111.9090	9.86	3.25
251	2011 01 26 05:10:11	42.4240	-111.4990	5.76	3.73
252	2011 03 16 19:09:36	44.6497	-112.0790	3.98	3.43

| | Moment Tensor Results | | | | | Ground Motions CY 2010 | |
M_w	Depth (km)	Strike1/2 (°)	Dip1/2 (°)	Rake1/2 (°)	Vs30 (m s^{-1})	PGA (cm s^{-2})	PGV (cm s^{-1})
					1460	2.65	0.05
					760	20.53	0.73
3.63	*10*	*179/5*	*55/35*	*-93/-85*	*709*	9.40	0.26
					592	4.86	0.12
4.47	5	52/170	77/27	-66/-150	1010	46.67	1.99
					1010	13.12	0.38
					1010	8.00	0.20
3.43	8	253/343	89/72	-18/-179	1010	7.01	0.17
3.39	5	180/51	57/46	-124/-49	1010	9.49	0.25
3.82	3	50/170	81/18	-74/-149	1010	25.38	0.91
					2197	7.46	0.18
					234	8.22	0.28
3.62	7	185/276	86/73	163/4	2197	10.09	0.26
					298	19.86	0.87

#	Origin Time	Latitude (°)	Longitude (°)	Depth (km)	M_L
253	2011 03 28 21:00:19	46.2705	-111.0890	6.7	3.05
254	2011 04 01 12:56:27	43.0293	-110.3120	0.24	4.22
255	2011 04 05 07:05:24	44.6630	-112.1650	0.94	4.57
256	2011 05 08 04:32:20	44.7977	-110.9850	5.4	3.15
257	2011 06 23 03:14:02	36.9723	-112.0940	6.61	3.35
258	2011 07 05 03:22:06	39.9303	-111.8210	6.51	3.19
259	2011 07 08 03:44:02	36.3185	-112.0390	2.45	3.23
260	2011 07 12 16:42:45	45.3638	-112.5840	0.19	3.22
261	2011 07 18 23:28:27	43.5078	-110.4240	0.07	3.17
262	2011 07 22 07:05:35	39.9320	-111.8230	5.25	3.3
263	2011 07 26 03:38:26	42.0522	-111.5580	1.1	3.65
264	2011 07 28 22:34:55	39.0007	-111.4980	0.67	3
265	2011 08 06 19:58:09	42.9500	-111.1380	0.04	3.03
266	2011 09 28 06:31:20	37.9097	-112.0540	6.86	3.49

	Moment Tensor Results					Ground Motions CY 2010	
M_w	Depth (km)	Strike1/2 (°)	Dip1/2 (°)	Rake1/2 (°)	Vs30 (m s^{-1})	PGA (cm s^{-2})	PGV (cm s^{-1})
					308	7.20	0.23
3.89	16	354/200	72/20	-99/-65	326	13.69	0.45
4.4	11	300/32	85/70	-20/-175	297	40.21	2.04
					565	7.78	0.22
					2197	6.84	0.16
					234	10.46	0.40
					366	17.49	0.70
					371	29.36	1.38
3.28	4	161/65	76/65	-154/-15	760	10.49	0.31
3.65	9	149/39	79/30	-118/-23	2197	8.63	0.21
3.6	7	357/196	58/34	-100/-74	2197	9.78	0.25
					1010	11.65	0.33
					596	18.46	0.68
3.67	16	205/12	54/37	-82/-100	234	11.06	0.37

Table B.1, continued

#	Origin Time	Latitude (°)	Longitude (°)	Depth (km)	M_L
267	2011 11 10 04:27:45	39.3025	-111.1510	5.63	3.9
268	2011 11 12 05:15:11	39.2255	-110.4540	12.86	3.16
269	2011 11 20 18:32:51	37.4287	-113.2250	4.48	3.01
270	2011 11 22 18:09:41	44.4577	-110.9770	0.88	3.06
271	2011 11 23 06:26:29	44.9468	-112.7280	1.12	3.41
272	2011 11 23 20:14:30	44.9430	-112.7280	0.97	3.24
273	2011 12 01 08:00:05	42.4722	-111.1910	6.44	3.05
274	2011 12 13 23:36:22	36.7403	-113.0400	5.68	3.09
275	2011 12 14 18:34:45	36.5595	-113.9000	6.32	3.45
276	2011 12 19 16:51:21	41.8092	-111.5830	4.42	3
277	2012 01 05 07:20:08	42.5312	-111.2330	0.67	3.46
278	2012 01 29 03:46:24	42.5212	-108.4360	2.37	3.24
279	2012 02 01 14:40:32	40.8420	-114.9930	7.07	3.63
280	2012 02 04 11:27:03	40.0182	-111.5250	8.8	3.64

| M_w | Depth (km) | Strike1/2 (°) | Dip1/2 (°) | Rake1/2 (°) | Vs30 (m s^{-1}) | Ground Motions CY 2010 | |
						PGA (cm s^{-2})	PGV (cm s^{-1})
		Moment Tensor Results					
3.96	4	234/329	79/68	158/12	1010	26.37	0.95
					1460	2.85	0.05
					234	10.21	0.39
					415	17.91	0.71
					557	26.26	1.08
					557	20.84	0.80
					1460	4.22	0.09
					302	8.85	0.30
					412	12.92	0.45
					1010	5.40	0.12
					606	30.65	1.29
					482	16.12	0.59
					271	18.66	0.81
3.67	9	172/262	90/81	171/0	1010	9.36	0.24

#	Origin Time	Latitude (°)	Longitude (°)	Depth (km)	M_L	M_w	Moment Tensor Results				Vs30 (m s^{-1})	Ground Motions CY 2010	
							Depth (km)	Strike1/2 (°)	Dip1/2 (°)	Rake1/2 (°)		PGA (cm s^{-2})	PGV (cm s^{-1})
281	2012 02 12 03:06:09	37.8552	-112.4040	0.53	3.18	3.53	3	167/41	84/10	-98/-36	234	29.91	1.59
282	2012 02 12 04:18:59	37.8558	-112.4050	0.07	3.5	3.67	10	158/6	53/40	-108/68	234	15.96	0.66
283	2012 02 16 08:20:58	39.6245	-111.5540	4.5	3.01						1010	5.42	0.12
284	2012 02 25 18:07:27	41.0760	-114.7370	7.14	3.07						*304*	7.12	0.23
285	2012 02 28 20:42:01	42.6693	-111.2430	1.26	3.35						*760*	20.23	0.71
286	2012 02 29 22:36:22	37.3592	-113.8420	1.32	3.05						2197	10.24	0.27
287	2012 03 09 01:08:34	42.9068	-111.2390	1.1	3.16						*690*	16.14	0.55
288	2012 03 23 18:04:42	45.4867	-112.1140	3.73	3.03						*760*	7.22	0.19
289	2012 03 29 17:22:06	38.9823	-111.3850	6.33	3.37						1460	7.31	0.17
290	2012 04 04 18:22:56	42.7752	-111.3340	4.87	3.1						*760*	6.78	0.17
291	2012 04 12 03:29:22	37.8257	-112.1150	5.1	4.13	4.13	11	162/28	52/48	-122/-55	1010	16.28	0.47
292	2012 05 02 13:10:07	41.4403	-110.7870	22	3.07						1010	1.75	0.02
293	2012 05 10 01:18:28	43.0497	-110.5100	0.59	3.56	3.56	9	50/141	85/75	-15/-175	*760*	8.89	0.24

REFERENCES

Allen, T.I., & Wald D.J., 2009. On the use of high-resolution topographic data as a proxy for seismic site conditions (VS30), *Bull. Seism. Soc. Am.*, **99**, 935–943.

Arrowsmith, S.J., & Whitaker, R.W., 2008. InfraMonitor: a tool for regional infrasound monitoring, in Proceedings of the 30th Monitoring Research Review: Ground-Based Nuclear Explosion Monitoring Technologies, Portsmouth, VA, September 23–25, LA-UR-08-05261, **2**, 837–843.

Arrowsmith, S.J., Whitaker, R.W., Katz, C. & Hayward, C., 2009. The F-detector revisited: an improved strategy for signal detection at seismic and infrasound arrays, *Bull. seism. Soc. Am.*, **99**(1), 449–453.

Arrowsmith, S.J., Johnson, B.J., Drob, D.P., & Hedlin, A.H., 2010. The seismoacoustic wavefield: A new paradigm in studying geophysical phenomena, *Rev. Geophys.*, **48**, RG4003, doi:10.1029/2010RG000335.

Arrowsmith, S.J., Burlacu, R., Pankow, K., Stump, B., Stead, R., Whitaker, R., & Hayward, C., 2012a. A seismoacoustic study of the 2011 January 3 Circleville earthquake, *Geophys. J. Int.*, **189**, 1148–1158, doi:10.1111/j.1365-246X.2012.05420.x.

Arrowsmith, S.J., 2012b. Users Guide of InfraMonitor3.1, 19 pp.

Benioff, H., & Gutenberg B., 1939. Waves and currents recorded by electromagnetic barographs, *Bull. Am. Meteorol. Soc.*, **20**, 421–426.

Burlacu, R., Arrowsmith, S.J., Pankow, K.L., Hale, J.M., Hayward, C., & Stump, B., 2010. A network of infrasound arrays in Utah, 2010 Fall Meeting, AGU, San Francisco, CA, 13–17 December.

Burlacu, R., Roberson, P.M., Hale, J.M., Gray, C., Willis, H., Koper, K.D., Pechmann, J.C., & Pankow, K.L., 2011. Earthquake activity in the Utah region: October 1–December 31, 2011, University of Utah Seismograph Stations Report, 46 pp.

Chiou, B.S.J., & Youngs, R.R., 2008. NGA ground motion model for the geometric mean horizontal component of peak and spectral ground motion parameters, *Earthquake Spectra*, **24**, 173–216.

Chiou, B.S.J., Youngs, R.R., Abrahamson, N.A., & Addo K., 2010. Ground-motion attenuation model for small-to-moderate shallow crustal earthquakes in California and its implications on regionalization of ground-motion prediction models, *Earthquake Spectra* **26**, 907–926.

Cook, R.K., 1971. Infrasound radiated during the Montana earthquake of 1959 August 18, *Geophys. J. R. astr. Soc.*, **26**, 191–198.

Drob, D.P., Picone, J.M., & Garcés, M., 2003. Global morphology of infrasound propagation, *J. Geophys. Res.*, **108**(D21), 4680, doi:10.1029/2002JD003307.

Garcia, R.F., Bruinsma, S., Lognonné, P., Doornbos, E., & Cachoux, F., 2013. GOCE: the first seismometer in orbit around the Earth, *Geophys. Res. Lett.*, **40**, 1015–1020, doi:10.1002/grl.50205.

Green, D.N., Guilbert, J., Le Pichon, A., Sebe, O. & Bowers, D., 2009. Modelling ground-to-air coupling for the shallow ML 4.3 Folkestone, United Kingdom, earthquake of 28 April 2007, *Bull. Seism. Soc. Am.*, **99**, 2541–2551, doi:10.1785/0120080236.

Gutenberg, B., 1939. The velocity of sound waves and the temperature in the stratosphere in southern California, *Bull. Am. Meteorol. Soc.*, **20**, 192–201.

Hale, J.M., Arrowsmith, S., Hayward, C., Burlacu, R., Pankow, K.L., Stump, B., Randall, G., & Taylor, S., 2010. Infrasound signal characteristics from small explosions, in Proceedings of the 32nd Monitoring Research Review: Ground-Based Nuclear Explosion Monitoring Technologies, Orlando, FL, September 21-23, LA-UR-10-05578, 720–730.

Hermann, R.B., Benz, H., & Ammon, C.J., 2011. Monitoring the earthquake source process in North America, *Bull. Seism. Soc. Am.,* **101,** doi:10.1785/0120110095.

Kim, T.S., Hayward, C., & Stump, B., 2004. Local infrasound signals from the Tokachi-Oki earthquake, *Geophys. Res. Lett.*, **31**, doi:10.1029/2004GL021178.

Le Pichon, A., Guilbert, J., Vega, A., Garces, M., & Brachet, N., 2002. Ground-coupled air waves and diffracted infrasound from the Arequipa earthquake of June 23, 2001, *Geophys. Res. Lett.,* **29,** 1886–1889.

Le Pichon, A., Mialle, P., Guilbert, J. & Vergoz, J., 2006. Multistation infrasonic observations of the Chilean earthquake of 2005 June 13, *Geophys. J. Int.*, **167**, 838–844.

McDonald, G.N., & Ashland, F.X., 2008. Earthquake site conditions in the Wasatch Front urban corridor, Utah: Utah Geological Special Study **125**, 41, 1 plate, scale 1:150,000, compact disk.

Minson, S.E., & Dreger, D.S., 2008. Stable inversions for complete moment tensors, *Geophys. J. Int.* **74**, 585–592.

Mutschlecner, J.P., Whitaker, R.W. & Auer, L.H., 1999. An empirical study of infrasonic propagation. Technical Report LA-13620-MS, Los Alamos National Laboratory, 69 pp.

Mutschlecner, J.P., & Whitaker, R.W., 2005. Infrasound from earthquakes, *J. Geophys. Res.*, **110**, doi:10.1029/2004JD005067.

Olson, J.V., Wilson, C.R., & Hansen, R., 2003. Infrasound associated with the 2002 Denali fault earthquake, Alaska, *Geophys. Res. Lett.*, **30**, doi:10.1029/2003GL018568.

Pankow, K.L., 2012. Instrumentally recorded ground motions in Utah region since 2000, *in* Hylland, M. D., & Harty, K. M., editors, Selected topics in engineering and environmental geology in Utah: Utah Geol. Assoc. Surv. Publ. **41**, 1–8.

ReVelle, D.O., Whitaker, R.W., Mutschlecner, J.P., & Renwald, M.D., 2004. Discrimination of earthquakes and mining blasts using infrasound in Proceedings of the 26th Monitoring Research Review, Orlando, FL, September 21-23, LA-UR-04-5801, 670–679.

Smith, R.B., & Arabasz, W.J., 1991, Seismicity of the Intermountain Seismic Belt, *in* Slemmons, D. B., Engdahl, E. R., Zoback, M. D., & Blackwell, D. D., eds., Neotectonics of North America: Boulder, Colorado, Geol. Soc. Am., Decade Map **1**, 185–228.

Stump, B., *et al.*, 2007. *Seismic and Infrasound Energy Generation and Propagation at Local and Regional Distances: Phase I – Divine Strake Experiment*, Technical Report to Air Force Research Laboratory under contract FA8718-06-C-0028, 23pp, Albuquerque, NM.

Wald, D.J., Worden, B.C., Quitoriano, V., & Pankow, K.L., 2003. ShakeMap Manual: Technical Manual, User's Guide, and Software Guide, Techniques and Methods U. S. Geological Survey Techniques and Methods, book 12, section A, Chap 1, CO 132 pp.

Walker, K.T., Shelby, R., Hedlin, M.A.H., de Groot-Hedlin, C., & Vernon, F., 2011. Western U.S. infrasonic catalog: Illuminating infrasonic hot spots with the USArray, *J. Geohys. Res.*, **116**, B12305, 15 pp, doi:10.1029/2011JB008579/.

Whidden, K.M., & Pankow K.L., 2012. A catalog of regional moment tensors in Utah from 1998 to 2011, *Seism. Res. Lett.*, **83,** 775–783, doi:10.1785/0220120046.